

**You might find this additional information useful...**

---

This article cites 67 articles, 44 of which you can access free at:

<http://ajprenal.physiology.org/cgi/content/full/281/2/F222#BIBL>

This article has been cited by 3 other HighWire hosted articles:

**A mathematical model of rat distal convoluted tubule. I. Cotransporter function in early DCT**

A. M. Weinstein

*Am J Physiol Renal Physiol*, October 1, 2005; 289 (4): F699-F720.

[\[Abstract\]](#) [\[Full Text\]](#) [\[PDF\]](#)

**A mathematical model of rat distal convoluted tubule. II. Potassium secretion along the connecting segment**

A. M. Weinstein

*Am J Physiol Renal Physiol*, October 1, 2005; 289 (4): F721-F741.

[\[Abstract\]](#) [\[Full Text\]](#) [\[PDF\]](#)

**Mathematical models of renal fluid and electrolyte transport: acknowledging our uncertainty**

A. M. Weinstein

*Am J Physiol Renal Physiol*, May 1, 2003; 284 (5): F871-F884.

[\[Abstract\]](#) [\[Full Text\]](#) [\[PDF\]](#)

Medline items on this article's topics can be found at <http://highwire.stanford.edu/lists/artbytopic.dtl> on the following topics:

Biochemistry .. Exchangers  
Biochemistry .. Transport Kinetics  
Biochemistry .. Transport Mechanism  
Physiology .. Water Transport  
Physiology .. Distal Convoluted Tubule  
Physiology .. Rats

Updated information and services including high-resolution figures, can be found at:

<http://ajprenal.physiology.org/cgi/content/full/281/2/F222>

Additional material and information about *AJP - Renal Physiology* can be found at:

<http://www.the-aps.org/publications/ajprenal>

---

This information is current as of November 27, 2009 .

# A numerical model of acid-base transport in rat distal tubule

HANGIL CHANG<sup>1</sup> AND TOSHIRO FUJITA<sup>2</sup>

<sup>1</sup>Health Service Center and <sup>2</sup>Department of Internal Medicine, University of Tokyo, Tokyo 153-8902, Japan

Received 10 July 2000; accepted in final form 22 February 2001

**Chang, Hangil, and Toshiro Fujita.** A numerical model of acid-base transport in rat distal tubule. *Am J Physiol Renal Physiol* 281: F222–F243, 2001.— The purpose of this study is to develop a numerical model that simulates acid-base transport in rat distal tubule. We have previously reported a model that deals with transport of Na<sup>+</sup>, K<sup>+</sup>, Cl<sup>-</sup>, and water in this nephron segment (Chang H and Fujita T. *Am J Physiol Renal Physiol* 276: F931–F951, 1999). In this study, we extend our previous model by incorporating buffer systems, new cell types, and new transport mechanisms. Specifically, the model incorporates bicarbonate, ammonium, and phosphate buffer systems; has cell types corresponding to intercalated cells; and includes the Na/H exchanger, H-ATPase, and anion exchanger. Incorporation of buffer systems has required the following modifications of model equations: new model equations are introduced to represent chemical equilibria of buffer partners [e.g., pH = pK<sub>a</sub> + log<sub>10</sub>(NH<sub>3</sub>/NH<sub>4</sub>)], and the formulation of mass conservation is extended to take into account interconversion of buffer partners. Furthermore, finite rates of H<sub>2</sub>CO<sub>3</sub>-CO<sub>2</sub> interconversion (i.e., H<sub>2</sub>CO<sub>3</sub> ⇌ CO<sub>2</sub> + H<sub>2</sub>O) are taken into account in modeling the bicarbonate buffer system. Owing to this treatment, the model can simulate the development of disequilibrium pH in the distal tubular fluid. For each new transporter, a state diagram has been constructed to simulate its transport kinetics. With appropriate assignment of maximal transport rates for individual transporters, the model predictions are in agreement with free-flow micropuncture experiments in terms of HCO<sub>3</sub><sup>-</sup> reabsorption rate in the normal state as well as under the high bicarbonate load. Although the model cannot simulate all of the micropuncture experiments, especially those that showed a flow-dependent increase in HCO<sub>3</sub><sup>-</sup> reabsorption, the model is consistent with those micropuncture experiments that showed HCO<sub>3</sub><sup>-</sup> reabsorption rates similar to those in the free-flow micropuncture experiments. We conclude that it is possible to develop a numerical model of the rat distal tubule that simulates acid-base transport, as well as basic solute and water transport, on the basis of tubular geometry, physical principles, and transporter kinetics. Such a model would provide a useful means of integrating detailed kinetic properties of transporters and predicting macroscopic transport characteristics of this nephron segment under physiological and pathophysiological settings.

bicarbonate transport; hydrogen ion transport; anion exchanger; hydrogen adenosinetriphosphatase; sodium-hydrogen exchanger

IN OUR PREVIOUS PAPER (22), we developed a numerical model of the rat distal tubule to help understand the

complex transport phenomena that had been observed in this nephron segment. In that study, we concentrated on transport of Na<sup>+</sup>, K<sup>+</sup>, Cl<sup>-</sup>, and water, because the magnitude of transport flux ascribable to these molecules overwhelms that of other molecules (such as H<sup>+</sup>, HCO<sub>3</sub><sup>-</sup>, Ca<sup>2+</sup>, Mg<sup>2+</sup>, ammonium, and phosphate). The distal tubule, however, actively participates in acidification of the tubular fluid, and normally it reabsorbs 5–10% of filtered HCO<sub>3</sub><sup>-</sup>, an amount equal to or greater than that assigned to the cortical and medullary collecting duct (16). In this paper, we extend our previous model to deal with acid-base transport in the rat distal tubule.

Acid-base transport in the rat distal tubule has been extensively studied by free-flow micropuncture and in vivo microperfusion experiments. These experiments have shown that there is an axial heterogeneity in the mechanism underlying transepithelial HCO<sub>3</sub><sup>-</sup> transport. In the early part of the distal tubule (that is, the distal convoluted tubule), H<sup>+</sup> is secreted into the tubular fluid via an Na/H exchanger located in the luminal membrane. Closely linked with this process, HCO<sub>3</sub><sup>-</sup> is transported out of the cytosolic space to the basolateral space, probably via an anion exchanger. In the late part, which is composed of the connecting tubule and the initial collecting tubule, there are distinct types of tubular cells (called intercalated cells) that are specifically involved in acid-base transport. One type of cell (type A intercalated cell) is involved in transepithelial HCO<sub>3</sub><sup>-</sup> reabsorption by secreting H<sup>+</sup> via luminal H-ATPase and extruding intracellular HCO<sub>3</sub><sup>-</sup> via the basolateral anion exchanger. Another type of cell (type B intercalated cell) has these transporters on the opposite side and secretes HCO<sub>3</sub><sup>-</sup> into the tubular fluid. These features of acid-base transport in the distal tubule are represented in the present model by introduction of new cell types that correspond to intercalated cells and new models of transporters that simulate transport kinetics of the Na/H exchanger, H-ATPase, and the anion exchanger. With the aid of a computer program (21) that solves steady-state equations of transitional state diagrams, we have been able to simulate transport kinetics of these transporters in a consistent manner.

The costs of publication of this article were defrayed in part by the payment of page charges. The article must therefore be hereby marked “advertisement” in accordance with 18 U.S.C. Section 1734 solely to indicate this fact.

Address for reprint requests and other correspondence: H. Chang, Health Service Center, Univ. of Tokyo, 3-8-1 Komaba, Meguro-ku, Tokyo 153-8902, Japan (E-mail: hchang-ky@umin.ac.jp).

As we did in the previous model, we adjust model parameters so that model predictions simulate the results of micropuncture experiments, because these experiments are the least invasive and yield mutually consistent results. Specifically, we try to fit the model to the results by Capasso et al. (16, 17): an  $\text{HCO}_3^-$  reabsorption rate of  $\sim 50$  pmol/min in normal rats and  $\sim 180$  pmol/min in acutely  $\text{HCO}_3^-$ -loaded rats. Additionally, we compare the model with in vivo micropuncture experiments. These experiments yield widely varied and mutually inconsistent results. For example, the  $\text{HCO}_3^-$  reabsorption rate in normal rats was essentially equal to zero in several reports (46, 56, 57), whereas it was comparable to micropuncture experiments in other reports (20, 54). The mechanism underlying the inconsistency has not been resolved and is possibly multifactorial, and we will make only a limited attempt to fit the model to micropuncture experiments.

## METHODS

**Model geometry and variables.** The model tubule has the same diameters (inner, 24  $\mu\text{m}$ ; outer, 37  $\mu\text{m}$ ) and length (0.23 cm) as in the previous model (22). Reflecting the axial heterogeneity of the actual tubule, the model is divided into two parts. The early (or upstream) part is 0.10 cm long and corresponds to the distal convoluted tubule (53). This portion is composed of a single type of cell (distal convoluted tubule cell). Accordingly, the model has only one cell type. The late part is 0.13 cm long and corresponds to the connecting tubule and the initial collecting tubule (53). This portion is composed of heterogeneous cell types. The predominant number of cells<sup>1</sup> is involved in  $\text{Na}^+$  and  $\text{K}^+$  transport and had been the only cell type incorporated in the previous model. Other cell types are type A intercalated cells and type B intercalated cells, which are involved in  $\text{H}^+$  secretion and  $\text{HCO}_3^-$  secretion, respectively. The present model incorporates both intercalated cell types. To derive the discretized form of the system of model equations that is suitable for numerical solution, the model tubule has been conceptually divided into 23 sections with equal widths (0.01 cm).

Model variables are composed of electrical potential, flow rate, and concentrations of  $\text{Na}^+$ ,  $\text{K}^+$ ,  $\text{Cl}^-$ ,  $\text{H}^+$ ,  $\text{HCO}_3^-$ ,  $\text{H}_2\text{CO}_3$ ,  $\text{NH}_4^+$ ,  $\text{NH}_3$ ,  $\text{H}_2\text{PO}_4^-$ ,  $\text{HPO}_4^{2-}$ , and urea in the luminal space; electrical potential and concentrations of  $\text{Na}^+$ ,  $\text{K}^+$ ,  $\text{Cl}^-$ ,  $\text{H}^+$ ,  $\text{HCO}_3^-$ ,  $\text{NH}_4^+$ ,  $\text{NH}_3$ , and impermeant solute in distal convoluted tubule cells and principal cells; and electrical potential and concentrations of  $\text{Cl}^-$ ,  $\text{H}^+$ ,  $\text{HCO}_3^-$ , and impermeant solute in intercalated cells. The total number of model variables (in the discretized form) has increased from 270 in the previous model to 611 in the present model.

**Model equations.** In the cellular compartments, mass conservation of water or solute is specified as

$$J_v^{\text{mc}} + J_v^{\text{sc}} = 0$$

$$J_x^{\text{mc}} + J_x^{\text{sc}} = 0$$

where  $J_v^{\text{mc}}$  is the volume flux from the luminal space into the cell,  $J_v^{\text{sc}}$  is the volume flux from the serosal space into the cell,  $J_x^{\text{mc}}$  is the flux of solute  $x$  from the luminal space into the cell,

and  $J_x^{\text{sc}}$  is the flux of solute  $x$  from serosal space into the cell. The iteration procedure of the Newton method (22), which has been used to solve the system of model equations, is continued until the absolute magnitude of the difference between the *left*-hand side and the *right*-hand side of each model equation becomes smaller than the tolerance value that is predetermined for each equation. The tolerance values for the above equations have been  $1.42 \times 10^{-7}$   $\text{ml}\cdot\text{s}^{-1}\cdot\text{cm}^{-2}$  and  $1.42 \times 10^{-10}$   $\text{mmol}\cdot\text{s}^{-1}\cdot\text{cm}^{-2}$ . These values have been selected to ensure that the sum of errors of all sections is, at most, 0.023 nl/min and 0.023 pmol/min. Conservation of solutes that constitute buffer systems is handled differently, as described later.

In the luminal compartment, mass conservation includes a convective term

$$\frac{dF_v}{dx} + 2\pi R_i J_v = 0$$

$$\frac{dF_x}{dx} + 2\pi R_i J_x = 0$$

where  $F_v$  is the tubular flow rate,  $R_i$  is the inner radius of the luminal compartment,  $J_v$  is the rate of transepithelial volume reabsorption,  $F_x$  is the flux of solute  $x$  along the tubular axis, and  $J_x$  is the rate of transepithelial reabsorption of solute  $x$ . If we neglect the electrodiffusive movement of solutes along the tubular axis,  $F_x$  is simply  $F_v C_x^{\text{m}}$ , where  $C_x^{\text{m}}$  is the concentration of solute  $x$  in the luminal compartment. The tolerance values have been  $1.7 \times 10^{-11}$  ml/s (0.001 nl/min) and  $1.7 \times 10^{-14}$  mmol/s (0.001 pmol/min). Conservation of solutes that constitute buffer systems are handled differently, as described later.

Electroneutrality within each compartment requires

$$\sum_x z_x C_x = 0$$

where  $z_x$  is the valence of solute  $x$ ,  $C_x$  is the concentration of solute  $x$  within the compartment, and the sum is of all the solutes within the compartment. The tolerance value has been 0.01 mM.

In the present model, introduction of buffer systems has required the following modifications of model equations. First, concentrations of the acid form ([Acid]) and the base form ([Base]) of a buffer system should fulfill the following condition

$$\text{pH} = \text{p}K_a + \log_{10} ([\text{Base}]/[\text{Acid}])$$

where  $\text{p}K_a = 10^{-K_a}$  ( $K_a$ : dissociation constant of the buffer system). The tolerance value has been 0.0001 pH unit.

Second, conservation of the total number of molecules that constitute a buffer system is considered, instead of individual molecular species. For example, in the case of the ammonium buffer system in the cytosolic space, the following equation has been postulated

$$J_{\text{NH}_4}^{\text{mc}} + J_{\text{NH}_3}^{\text{mc}} + J_{\text{NH}_4}^{\text{sc}} + J_{\text{NH}_3}^{\text{sc}} = 0$$

where  $J_{\text{NH}_4}^{\text{mc}}$  and  $J_{\text{NH}_3}^{\text{mc}}$  are fluxes of  $\text{NH}_4^+$  and  $\text{NH}_3$  from the luminal space into the cell, and  $J_{\text{NH}_4}^{\text{sc}}$  and  $J_{\text{NH}_3}^{\text{sc}}$  are fluxes from the serosal space, respectively. The above equation is derived from the fact that the amount of  $\text{NH}_4^+$  generated by the chemical reaction ( $\text{NH}_3 + \text{H}^+ \rightleftharpoons \text{NH}_4^+$ ) is exactly the same as the amount of  $\text{NH}_3$  consumed in the reaction.

Third, the model equation that represents mass conservation of  $\text{H}^+$  includes the term of the rate of  $\text{H}^+$  generation via interconversion of buffer partners ( $\text{Base} + \text{H}^+ \rightleftharpoons \text{Acid}$ ). For

<sup>1</sup>They are connecting tubule cells in the connecting tubule and principal cells in the initial collecting tubule. Hereafter, they are collectively referred to as "principal cells."

example, the equation of mass conservation of  $H^+$  in the luminal space becomes

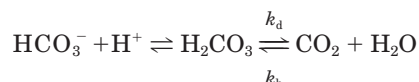
$$\frac{dF_H}{dx} + 2\pi R_l J_H - \pi R_l^2 G_H = 0 \quad (1)$$

where  $F_H$  is the flux of  $H^+$  along the tubular axis,  $J_H$  is the rate of transepithelial efflux of  $H^+$ , and  $G_H$  is the rate of  $H^+$  generation via interconversion of buffer partners. This equation can be used as a model equation without the introduction of a new model variable ( $G_H$ ), because  $G_H$  can be expressed by model variables as follows.<sup>2</sup> When there is only one buffer system, it can be easily deduced that  $G_{Base} = G_H = -G_{Acid}$ . When there are more than one buffer system, the relationship becomes

$$G_H = \sum G_{Base}$$

where the sum on the *right*-hand side encompasses all the bases (that is,  $HCO_3^-$ ,  $NH_3$ , and  $HPO_4^{2-}$  in this model).  $G_{Base}$  can be expressed in terms of model variables using the equation similar to Eq. 1. Consequently,  $G_H$  can be expressed in terms of model variables.

Last, finite rates of  $H_2CO_3$  dehydration and  $CO_2$  hydration are taken into account in modeling the bicarbonate buffer system. The bicarbonate buffer system is composed of  $HCO_3^-$ ,  $H_2CO_3$ , and  $CO_2$ , which are interconverted according to the following reaction<sup>3</sup>



The *left* part of the reaction is a rapid process and is essentially at equilibrium. Therefore, given the  $pK_a$  of 3.57 for carbonic acid, the following relationship can be assumed

$$pH = 3.57 + \log_{10} \frac{[HCO_3^-]}{[H_2CO_3]} \quad (2)$$

In contrast, the *right* part of the reaction is a slower process,<sup>4</sup> and  $H_2CO_3$  concentration can deviate significantly from its equilibrium value when there is an  $H^+$  load. For example, when there is an  $H^+$  load of  $0.8 \times 10^{-3} \text{ mmol} \cdot \text{s}^{-1} \cdot \text{cm}^{-3}$  (which is equivalent to  $50 \text{ pmol} \cdot \text{min}^{-1} \cdot \text{distal tubule}^{-1}$ ) in the absence of carbonic anhydrase activity, luminal  $H_2CO_3$  concentration should increase<sup>5</sup> by  $16 \text{ } \mu\text{M}$  from its equilibrium value ( $k_h/k_d[CO_2] = 3.6 \text{ } \mu\text{M}$ ). Owing to this increase in  $H_2CO_3$  concentration, the pH value becomes lower (Eq. 2) than the value observed when there is no  $H^+$  load. The difference is called "disequilibrium pH" and is demonstrated experimentally in the distal tubule (62). Disequilibrium pH is simulated in the present model by formulating the following model equation that relates the rate of  $H_2CO_3$  generation and the rate of  $HCO_3^-$  generation, which is equivalent to Eq. 7 in Ref. 78

$$G_{H_2CO_3} = -G_{HCO_3^-} - k_d \cdot [H_2CO_3] + k_h \cdot [CO_2] \quad (3)$$

<sup>2</sup> $F_H$  and  $J_H$  can be expressed in terms of model variables as shown in our previous study (22).

<sup>3</sup>The model does not incorporate  $CO_3^{2-}$ , because this component is negligible at physiological pH.

<sup>4</sup>According to Garg and Maren (35), the rate constant of carbonic acid dehydration ( $k_d$ ) is  $49.6 \text{ s}^{-1}$ , and the rate constant of  $CO_2$  hydration ( $k_h$ ) is  $0.145 \text{ s}^{-1}$  at  $37^\circ\text{C}$ .

<sup>5</sup>Throughout the study,  $CO_2$  concentration ( $[CO_2]$ ) is assumed to be  $1.2 \text{ mM}$ , corresponding to  $PCO_2$  of 40 Torr. This assumption is based on the experimental observation that there is no detectable difference in  $PCO_2$  between cortical structures of the kidney and the arterial blood (26). See DISCUSSION for details.

The tolerance value has been  $3.7 \text{ mmol} \cdot \text{s}^{-1} \cdot \text{cm}^{-3}$  (equivalent to  $0.0001 \text{ pmol} \cdot \text{min}^{-1} \cdot \text{section}^{-1}$ ). In the present model, disequilibrium pH exists only in the luminal space. In the cytosolic space, we have assumed that  $H_2CO_3$  concentration is essentially equal to the equilibrium value ( $3.6 \text{ } \mu\text{M}$ ) due to the carbonic anhydrase in the distal tubular cells (27). Consequently, cytosolic  $H_2CO_3$  concentration is equal to the serosal  $H_2CO_3$  concentration (which is also equal to the equilibrium value), and there would be no  $H_2CO_3$  transport across basolateral cell membranes even if there is  $H_2CO_3$  permeability. Therefore, basolateral  $H_2CO_3$  permeability is not incorporated in the present model.

The model equations have been transformed to a system of difference equations and solved numerically. The derivation of difference equations has been conducted as in the previous study (22). Briefly, the model tubule has been divided into 23 sections, and the continuous model variables have been replaced by discrete ones that represent the values at the center of each section. Previously, we had compared two separate derivations of difference equations: one taking into account the axial electrodiffusive movement of molecules and another neglecting it. The derivation with electrodiffusive terms had the advantage of being a more realistic prediction of luminal electrical potential profile at the junction of the early and late distal tubules but had the disadvantage of demanding an  $\sim 35$  times longer computational time. In the present study, we have employed only the derivation without electrodiffusive terms, because solution of the equations with electrodiffusive terms has become prohibitively time-consuming due to the increased number of model variables and more involved calculations of transport velocities through transporters (as described below). Fortunately, model predictions relevant to the present study (that is, reabsorption rates of solute and water) had been essentially unaffected by the choice of the discretization schemes (22). The present program solves the model equation in  $\sim 910 \text{ ms}$  when run on a machine with PowerPC 604e (180-MHz clock cycle).

### Transporters

Transporters that have been incorporated into the present model are illustrated in Figs. 1 and 2. In the early distal tubule (Fig. 1), distal convoluted tubule cells have a Na-Cl cotransporter, Na/H exchanger, K-Cl cotransporter,  $Na^+$  channel,  $K^+$  channel (also permeable for  $NH_4^+$ ),  $Cl^-$  channel,  $NH_3$  permeability,  $H_2CO_3$  permeability (not listed in Fig. 1), and H-ATPase in the luminal membrane; and Na-K-ATPase, an anion exchanger,  $K^+$  channel (also permeable for  $NH_4^+$ ),  $Cl^-$  channel, and  $NH_3$  permeability in the basolateral membrane. The paracellular pathway has conductances for  $Na^+$ ,  $K^+$ ,  $NH_4^+$ ,  $Cl^-$ , and  $HCO_3^-$  ions. In the late distal tubule (Fig. 2), principal cells have the Na-Cl cotransporter, K-Cl cotransporter,  $Na^+$  channel,  $K^+$  channel (also permeable for  $NH_4^+$ ),  $Cl^-$  channel,  $NH_3$  permeability, and  $H_2CO_3$  permeability (not listed in Fig. 2) in the luminal membrane; and Na-K-ATPase, an Na/H exchanger, anion exchanger,  $K^+$  channel (also permeable for  $NH_4^+$ ),  $Cl^-$  channel, and  $NH_3$  permeability in the basolateral membrane. Type A intercalated cells have H-ATPase in the luminal membrane and an anion exchanger and  $Cl^-$  channel in the basolateral membrane. Type B intercalated cells have an anion exchanger in the luminal membrane and H-ATPase and  $Cl^-$  channel in the basolateral membrane. The paracellular pathway has the same conductances as in the early distal tubule.

Transport velocities via the K-Cl cotransporter, ion channels, and paracellular conductances have been calculated as in the previous model (22). Briefly, transport velocity via the K-Cl cotransporter has been calculated by an equation derived from a kinetic diagram that accounts for apparent

Early Distal Tubule

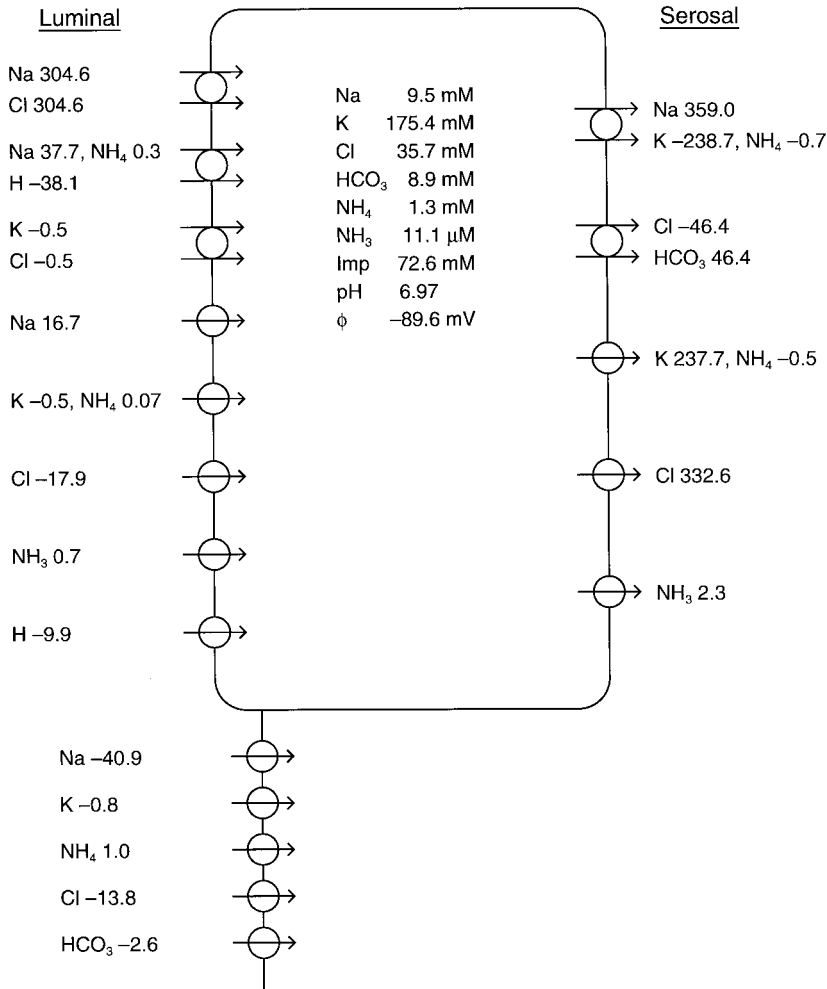


Fig. 1. Transport mechanisms of the early distal tubule. Distal convoluted tubule cell is represented as a large rectangle. In the luminal cell membrane, there are (from top to bottom) thiazide-sensitive Na-Cl cotransporter, Na/H exchanger, K-Cl cotransporter, Na<sup>+</sup> channel, K<sup>+</sup> channel (also permeable for NH<sub>4</sub><sup>+</sup>), Cl<sup>-</sup> channel, permeability for H<sub>2</sub>CO<sub>3</sub> (not listed), permeability for NH<sub>3</sub>, and H-ATPase. In the basolateral cell membrane, there are Na-K-ATPase, anion exchanger, K<sup>+</sup> channel (also permeable for NH<sub>4</sub><sup>+</sup>), Cl<sup>-</sup> channel, and permeability for NH<sub>3</sub>. In the tight junction (paracellular pathway), there are conductances for Na<sup>+</sup>, K<sup>+</sup>, NH<sub>4</sub><sup>+</sup>, Cl<sup>-</sup>, and HCO<sub>3</sub><sup>-</sup>. Alongside of circles indicating individual transport mechanisms, transport velocities in the basic state are expressed as pmol/min. φ, Electrical potential.

dissociation constants for K<sup>+</sup> and Cl<sup>-</sup> (38); and transport velocities via ion channels and paracellular conductances have been calculated by the Goldman-Hodgkin-Katz current equation (41). In the present model, we have assumed that the K<sup>+</sup> channel is also permeable for NH<sub>4</sub><sup>+</sup>, because the ROMK channel, which is the native K<sup>+</sup> channel in principal cells of the cortical collecting duct, has been demonstrated to be permeable for NH<sub>4</sub><sup>+</sup> (66). On the basis of the single-channel conductances and channel open probabilities for K<sup>+</sup> and NH<sub>4</sub><sup>+</sup>, we have assumed that the magnitude of NH<sub>4</sub><sup>+</sup> permeability,  $P_{NH_4}$ , is 20% of K<sup>+</sup> permeability,  $P_K$  (66, 78). We have also assumed that NH<sub>4</sub><sup>+</sup> is permeable through the tight junction with permeability similar to that for other cations. Transport rates of water across cell membranes have been assumed to be proportional to the difference in osmolarity across the membrane.

Calculation of transport velocity via the Na-Cl cotransporter [thiazide-sensitive Na-Cl cotransporter (TSC)] has been extended from the previous model to simulate a wider range of experimental observations as described in Chang and Fujita (21). The extended model simulates those experimental data of TSC, such as binding of thiazide in the absence of substrates, inhibitory effect of Cl<sup>-</sup> on thiazide binding, stimulatory effect of Na<sup>+</sup> on thiazide binding, combined effects of Na<sup>+</sup> and Cl<sup>-</sup> on thiazide binding, dependence of Na<sup>+</sup> influx on extracellular Na<sup>+</sup> and Cl<sup>-</sup>, and inhibition of

Na<sup>+</sup> influx by extracellular thiazide (21). To be consistent with the previous model parameters, transport velocity via TSC ( $J_{TSC}$ ) has been represented in the following form

$$J_{TSC} = J_{TSC, \max} \frac{j_{TSC}}{j_{TSC, \max}}$$

where  $J_{TSC, \max}$  (mmol·s<sup>-1</sup>·cm<sup>-2</sup>) is a model parameter,  $j_{TSC}$  is the transport velocity via a single TSC molecule, and  $j_{TSC, \max}$  is the maximal transport velocity via a single TSC molecule. In this way, model parameter  $J_{TSC, \max}$  represents the maximal transport rate that is achievable via the TSC transport mechanism as in the previous presentation. This convention has also been followed by other transporters that have been newly introduced.

Calculation of transport velocities via Na-K-ATPase has been extended to include NH<sub>4</sub><sup>+</sup> transport (75). Specifically, transport velocities of NH<sub>4</sub><sup>+</sup> ( $J_{NH_4-ATPase}$ ) and K<sup>+</sup> ( $J_{K-ATPase}$ ) have been calculated from the following equations (78)

$$J_{K-ATPase} + J_{NH_4-ATPase} = 2 \cdot J_a$$

$$J_{K-ATPase} : J_{NH_4-ATPase} = \frac{C_K^s}{K_K} : \frac{C_{NH_4}^s}{K_{NH_4}}$$

where  $J_a$  is the rate of ATP hydrolysis,  $C_K^s$  and  $C_{NH_4}^s$  are basolateral K<sup>+</sup> and NH<sub>4</sub><sup>+</sup> concentrations, and  $K_K$  and  $K_{NH_4}$

Late Distal Tubule

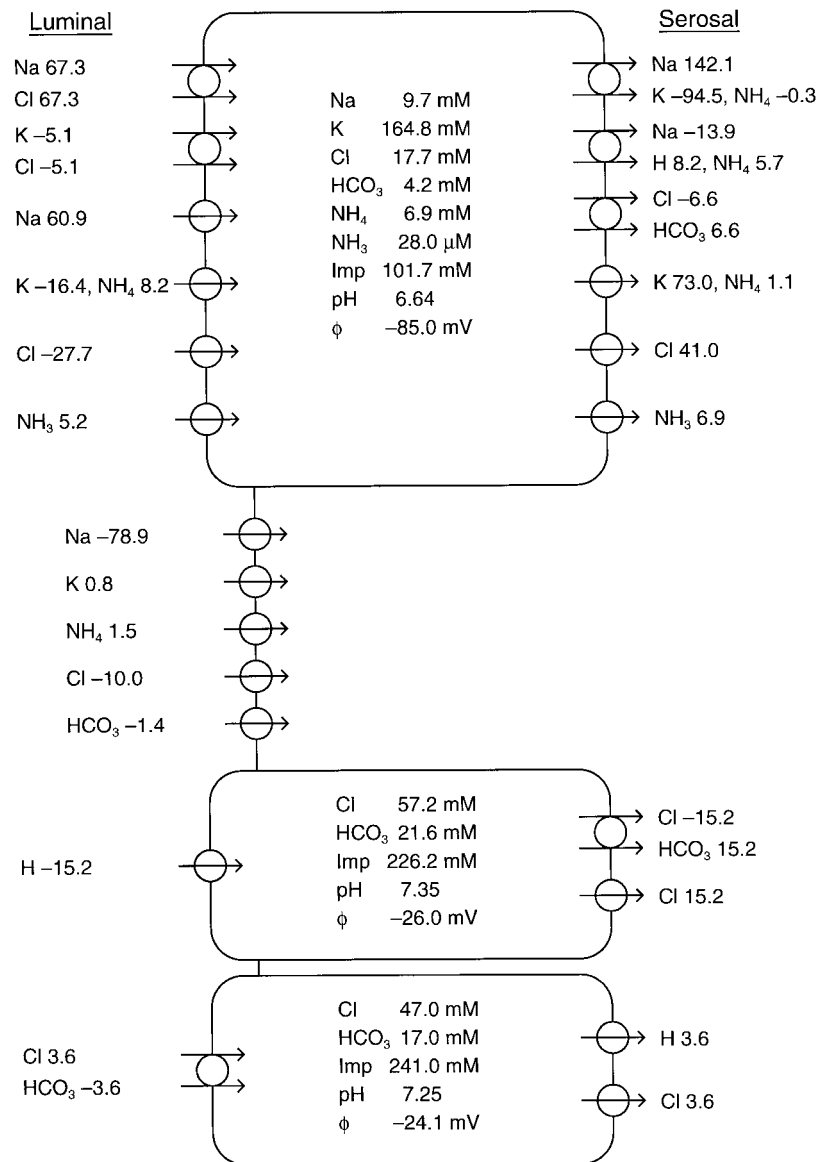


Fig. 2. Transport mechanisms of the late distal tubule. From the top of the figure, principal cell, type A intercalated cell, and type B intercalated cell are represented by rectangles. In the luminal cell membrane of principal cells, there are (from top to bottom) thiazide-sensitive Na-Cl cotransporter, K-Cl cotransporter, Na<sup>+</sup> channel, K<sup>+</sup> channel (also permeable for NH<sub>4</sub><sup>+</sup>), Cl<sup>-</sup> channel, permeability for H<sub>2</sub>CO<sub>3</sub> (not listed), and permeability for NH<sub>3</sub>. In the basolateral side of principal cells, there are Na-K-ATPase, Na/H exchanger, anion exchanger, K<sup>+</sup> channel (also permeable for NH<sub>4</sub><sup>+</sup>), Cl<sup>-</sup> channel, and permeability for NH<sub>3</sub>. In the tight junction, there are conductances for Na<sup>+</sup>, K<sup>+</sup>, NH<sub>4</sub><sup>+</sup>, Cl<sup>-</sup>, and HCO<sub>3</sub><sup>-</sup>. In type A intercalated cells, there is H-ATPase on the luminal side; and there are anion exchanger and Cl<sup>-</sup> channel on the basolateral side. In type B intercalated cells, there is anion exchanger on the luminal side; and there are H-ATPase and Cl<sup>-</sup> channel on the basolateral side. Alongside of circles indicating individual transport mechanisms, transport velocities in the basic state are expressed as pmol/min.

are kinetic constants with the ratio ( $K_{NH_4}/K_K$ ) of 5.8 (75). With typical values of basolateral K<sup>+</sup> concentration (4.25 mM) and NH<sub>4</sub><sup>+</sup> concentration (0.068 mM; Ref. 44),  $J_{NH_4-ATPase}/J_{K,ATPase}$  becomes 0.0028. The rate of ATP hydrolysis ( $J_a$ ) and transport velocity of Na<sup>+</sup> ( $J_{Na-ATPase}$ ) have been calculated as before (22, 83)

$$J_a = J_{a, \max} \cdot \frac{1}{1 + \left(\frac{K_{Na, ATPase}}{C_{Na}^c}\right)^3}$$

$$J_{Na-ATPase} = -3 \cdot J_a$$

where  $J_{a, \max}$  is a model parameter,  $C_{Na}^c$  is cytosolic Na<sup>+</sup> concentration, and  $K_{Na-ATPase}$  is a kinetic constant with a value of 12 mM.

Transport velocities via NH<sub>3</sub> permeability and H<sub>2</sub>CO<sub>3</sub> permeability have been assumed to be proportional to concentration differences

$$J_{NH_3} = P_{NH_3} \cdot ([NH_3]_{from} - [NH_3]_{to})$$

$$J_{H_2CO_3} = P_{H_2CO_3} \cdot ([H_2CO_3]_{from} - [H_2CO_3]_{to})$$

Transport via the Na/H exchanger has been assumed to obey a kinetic diagram (Fig. 3 and Table 1) that is based on the one elaborated by Weinstein (77). In this diagram, the Na/H exchanger has a single binding site to which Na<sup>+</sup>, H<sup>+</sup>, and NH<sub>4</sub><sup>+</sup> competitively bind, and only the bound forms of the transporter are able to cross the membrane. One noticeable feature of this model is that transitional rate constants are symmetrical with respect to the membrane (for example,  $k_1 = k_7$ ,  $k_2 = k_8$ , and  $k_{13} = k_{14}$ ; Fig. 3 and Table 1). Besides the benefit of decreasing the number of independent param-

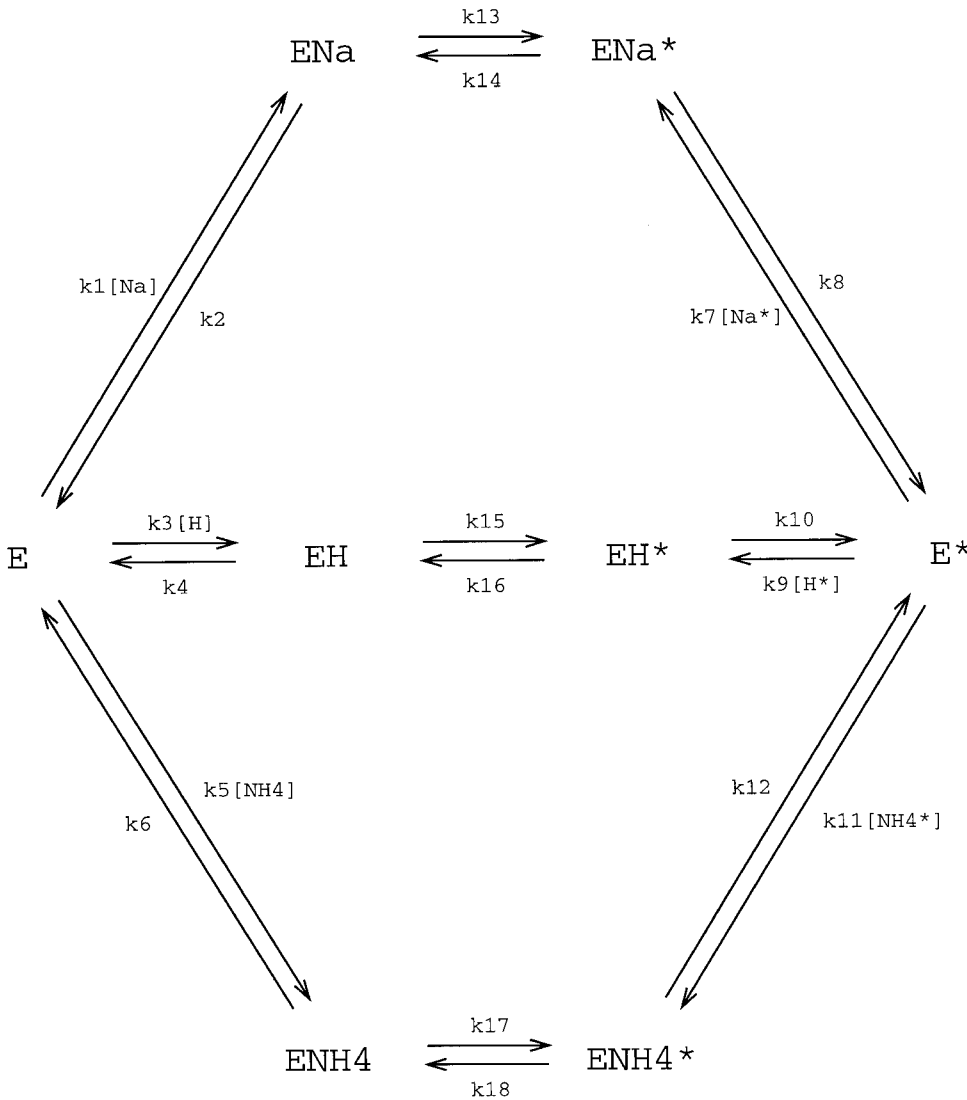


Fig. 3. State diagram of Na-H exchanger. The model Na-H exchanger (E) has a single binding site to which Na<sup>+</sup>, H<sup>+</sup>, and NH<sub>4</sub><sup>+</sup> bind competitively. Only loaded transporters (ENa, EH and ENH4 in the extracellular side; and ENa\*, EH\*, and ENH4\* in the intracellular side) can cross the membrane. Bracketed symbols (such as [H] and [Na\*]) indicate substrate concentrations.

Table 1. Rate constants of Na/H exchanger

$k_1$	$1.00 \times 10^8$	$\text{cm}^3 \cdot \text{mmol}^{-1} \cdot \text{s}^{-1}$
$k_2$	$3.27 \times 10^6$	$\text{s}^{-1}$
$k_3$	$1.00 \times 10^8$	$\text{cm}^3 \cdot \text{mmol}^{-1} \cdot \text{s}^{-1}$
$k_4$	$3.52 \times 10^0$	$\text{s}^{-1}$
$k_5$	$1.00 \times 10^8$	$\text{cm}^3 \cdot \text{mmol}^{-1} \cdot \text{s}^{-1}$
$k_6$	$7.13 \times 10^5$	$\text{s}^{-1}$
$k_7$	$1.00 \times 10^8$	$\text{cm}^3 \cdot \text{mmol}^{-1} \cdot \text{s}^{-1}$
$k_8$	$3.27 \times 10^6$	$\text{s}^{-1}$
$k_9$	$1.00 \times 10^8$	$\text{cm}^3 \cdot \text{mmol}^{-1} \cdot \text{s}^{-1}$
$k_{10}$	$3.52 \times 10^0$	$\text{s}^{-1}$
$k_{11}$	$1.00 \times 10^8$	$\text{cm}^3 \cdot \text{mmol}^{-1} \cdot \text{s}^{-1}$
$k_{12}$	$7.13 \times 10^5$	$\text{s}^{-1}$
$k_{13}$	$2.41 \times 10^0 \times W^*$	$\text{s}^{-1}$
$k_{14}$	$2.41 \times 10^0 \times W^*$	$\text{s}^{-1}$
$k_{15}$	$4.80 \times 10^{-1} \times W^*$	$\text{s}^{-1}$
$k_{16}$	$4.80 \times 10^{-1} \times W^*$	$\text{s}^{-1}$
$k_{17}$	$2.41 \times 10^0 \times W^*$	$\text{s}^{-1}$
$k_{18}$	$2.41 \times 10^0 \times W^*$	$\text{s}^{-1}$

\*Rates of translocation of loaded Na/H exchanger (from  $k_{13}$  through  $k_{18}$ ) are modified by a factor of  $W = \frac{[\text{H}^*]}{([\text{H}^*] + K_H)}$ , where  $[\text{H}^*]$  is the concentration of internal H<sup>+</sup>, and  $K_H = 1 \mu\text{M}$  (77).

eters, this feature ensures that thermodynamic requirements (55) such as  $k_1 k_4 k_8 k_9 k_{13} k_{16} = k_2 k_3 k_7 k_{10} k_{14} k_{15}$  are automatically fulfilled. Another feature (described in Table 1) is that rates of translocation (from  $k_{13}$  through  $k_{18}$ ) are affected by cytosolic H<sup>+</sup> concentration (for quantitative description, see the legend for Table 1). This aspect of the model (internal modifier site) was necessary (77) to account for the observed complex effect of internal H<sup>+</sup> on net transport, with intracellular alkalosis shutting off Na/H exchange more sharply than a simple substrate depletion effect (4).

Transport velocity via the Na/H exchanger can be calculated by numerically solving the steady-state equations of this diagram by using the program that we had developed (21). With an internal pH of 6.0 (and no internal Na<sup>+</sup>), Na<sup>+</sup> influx of the model Na/H exchanger has an apparent  $K_{\text{Na}}$  of 58.8 mM when external pH is 6.6 and 11.9 mM when external pH is 7.5, whereas the corresponding experimental values are 54 and 13 mM (5), respectively. The inhibition constant ( $K_i$ ) for inhibition of Na<sup>+</sup> influx by external H<sup>+</sup> (external Na<sup>+</sup> 0.1 mM; internal Na<sup>+</sup> 0 mM; and internal pH 6.0) is 38 nM, and the corresponding experimental value is 35 nM (5).  $K_i$  for inhibition of Na<sup>+</sup> influx by external NH<sub>4</sub><sup>+</sup> (external Na<sup>+</sup> 0.1 mM; internal Na<sup>+</sup> 0 mM; and internal pH 6.0) is 50 mM when

external pH is 6.6 and 11 mM when external pH is 7.5, both of which are identical to experimental values (5).

The kinetic model of H-ATPase is from Andersen et al. (3). This model had been developed to explain the relationship between transport velocity via H-ATPase and luminal pH in the turtle bladder (see Fig. 5 in Ref. 3). According to this model, H-ATPase consists of two components (Fig. 4): a catalytic unit at the cytoplasmic side that mediates the ATP-driven  $H^+$  translocation, and a transmembrane channel that mediates the transfer of  $H^+$  from the catalytic unit to the extracellular solution. Between these two compartments there exists a buffer compartment (antechamber; Fig. 4), in which  $H^+$  is nearly in equilibrium with extracellular  $H^+$ . The catalytic unit has two binding sites for  $H^+$ , and only the fully loaded form can translocate  $H^+$  from the cytosolic space to the antechamber (Fig. 5). Therefore, stoichiometry is strictly  $2H^+ : 1ATP$ .

Values of rate constants for the kinetic model of H-ATPase are listed in Table 2, which are essentially identical to the ones reported by Andersen et al. (3). These values fulfill the thermodynamic requirement

$$k_1 k_3 k_6 k_8 k_{10} k_{11} / k_2 k_4 k_5 k_7 k_9 k_{12} = \exp(\Delta G_{ATP}^0 / RT)$$

where  $\Delta G_{ATP}^0$  is the standard free energy change of ATP hydrolysis ( $-33$  kJ/mol). We have assumed that cytosolic ATP concentration  $[ATP]_c = 2.5 \times 10^{-3}$  M, and  $[ADP]_c \cdot [P_i]_c = 10^{-7}$  M<sup>2</sup> (3). Transport velocity through H-ATPase has been calculated by solving the steady-state equations of the kinetic diagram. Transport velocity of the model H-ATPase is plotted in Fig. 6 as a function of luminal pH. The continuous line represents the calculation that simulates the experiments by Andersen et al. (3). The model prediction fits well with the experimental data (● in Fig. 6). Transport velocity becomes half-maximal near the luminal pH of 6.0, and it becomes essentially undetectable at a luminal pH of 4 (0.5% of the maximal rate). At a luminal pH of 3.2,  $H^+$

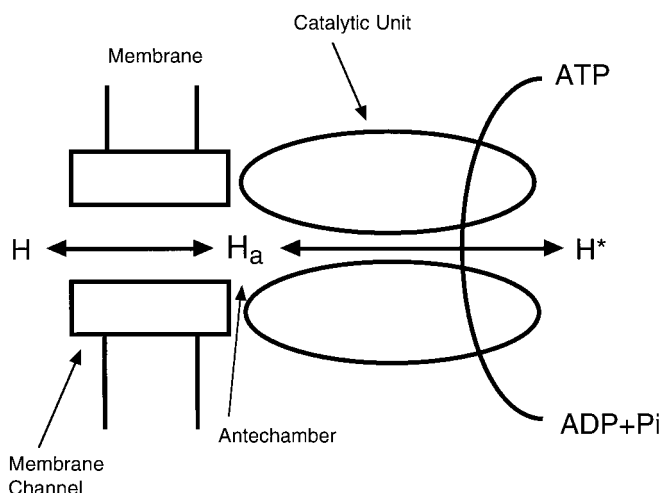


Fig. 4. Conceptual diagram of H-ATPase. The transporter consists of 2 components: a membrane channel and a catalytic unit. Between these components, there is a buffer space (antechamber), in which hydrogen ion ( $H_a$ ) is essentially in equilibrium with extracellular hydrogen ion ( $H$ ) owing to a large conductance of the membrane channel. Hydrogen ion in the antechamber is also interchangeable with cytosolic hydrogen ion ( $H^*$ ) through the catalytic unit. This process is coupled with ATP hydrolysis/synthesis with a stoichiometry of  $2H^+ : 1ATP$ .

transport reverses its direction.<sup>6</sup> In Fig. 6, transport velocities under the conditions simulating distal convoluted tubule cells and type A intercalated cells are also shown (dashed lines).

A state diagram for the anion exchanger, which catalyzes one-for-one exchange of anions such as  $Cl^-$  and  $HCO_3^-$ , is illustrated in Fig. 7. In this diagram, termed the “ping-pong” mechanism by Gunn and Frölich (43), the anion exchanger has a single binding site (transport site) to which substrates ( $Cl^-$  and  $HCO_3^-$ ) competitively bind, and only loaded transporters can cross the membrane. Additionally, there is an internal modifier site to which cytosolic  $Cl^-$  and  $HCO_3^-$  competitively bind. Binding to this modifier site is independent of the state of the transport site, and the anion exchanger with the modifier site occupied cannot participate in ion transport. Therefore, the transport rate is decreased by a factor of  $(1 + [Cl^*]/K_i^{Cl} + [HCO_3^*]/K_i^{HCO_3})^{-1}$ , where  $[Cl^*]$  is the cytosolic  $Cl^-$  concentration,  $[HCO_3^*]$  is the cytosolic  $HCO_3^-$  concentration,  $K_i^{Cl}$  is the dissociation constant of the modifier site for  $Cl^-$ , and  $K_i^{HCO_3}$  is the dissociation constant for  $HCO_3^-$ .

Values of rate constants for anion exchanger are listed in Table 3. We have assumed that rate constants involved in substrate binding ( $k_1$ ,  $k_3$ ,  $k_5$ , and  $k_7$ ) are diffusion limited (45). We have also assumed that affinities of the transport site for  $Cl^-$  and  $HCO_3^-$  are symmetrical with respect to the cell membrane, according to the report by Liu et al. (59). Other rate constants have been optimized by Powell’s method (69) to fit the experimental results of Gasbjerg et al. (36) and Knauf et al. (49), who investigated the kinetics of the anion exchanger in human red blood cells at body temperature ( $38^\circ C$ ). We note that rate constants for  $Cl^-$  dissociation ( $k_2$  and  $k_6$ ) are consistent with the lower limits of these values determined by <sup>35</sup>Cl NMR ( $4.5 \times 10^5$  s<sup>-1</sup> for  $k_2$  and  $1.3 \times 10^5$  s<sup>-1</sup> for  $k_6$ ; Ref. 31). Model predictions with these rate constants, together with experimental data, are plotted in Figs. 8 and 9. The model anion exchanger simulates dependency of transport velocity on extracellular and intracellular  $HCO_3^-$  concentrations (Fig. 8) and dependency of transport velocity on extracellular and intracellular  $Cl^-$  concentrations (Fig. 9). A similar kinetic model of the anion exchanger that also fits well to these experimental results has been recently reported by Weinstein (79).

From Table 3, we can see that loaded transporters translocate faster to the intracellular side than to the extracellular side (that is,  $k_9 > k_{10}$  and  $k_{11} > k_{12}$ ). This indicates that the anion exchanger is more stable in the intracellular side than in the extracellular side when substrate concentrations are equal on both sides of the membrane. Quantitatively, this is represented by the asymmetry factor ( $A$ ) that is defined as the ratio of unloaded outward-facing sites to unloaded inward-facing sites,  $[E]/[E^*]$ , with equal concentrations of substrates. According to the ping-pong model (as is the present model),  $A$  should be the same regardless of concentrations and species of the substrate that are used to measure it,

<sup>6</sup>This property of the model H-ATPase is consistent with the following calculation. Free energy change of ATP hydrolysis ( $\Delta G$ ) is calculated to be  $\Delta G_{ATP}^0 + RT \log([ADP][P_i]/[ATP]) = -59$  kJ/mol, which is similar to the values measured in various tissues including the kidney (55). Due to the stoichiometry of  $2H^+ : 1ATP$ ,  $\sim 30$  kJ is used to transport 1 mole of  $H^+$ . Therefore, the lower limit of luminal pH is estimated to be  $\sim 3.2$  from the equation,  $RT \log([H^+]_m/[H^+]_c) = \Delta G_2 - F(\psi_m - \psi_c)$ , where  $[H^+]_m$  and  $[H^+]_c$  are  $H^+$  concentrations in luminal space and intracellular space,  $F$  is the Faraday constant, and  $\psi_m$  and  $\psi_c$  are luminal and cytosolic electrical potential, respectively. In this calculation, we have assumed (3)  $\psi_m = 0$ ;  $\psi_c = -30$  mV; and  $-\log[H^+]_c = 7.5$ .

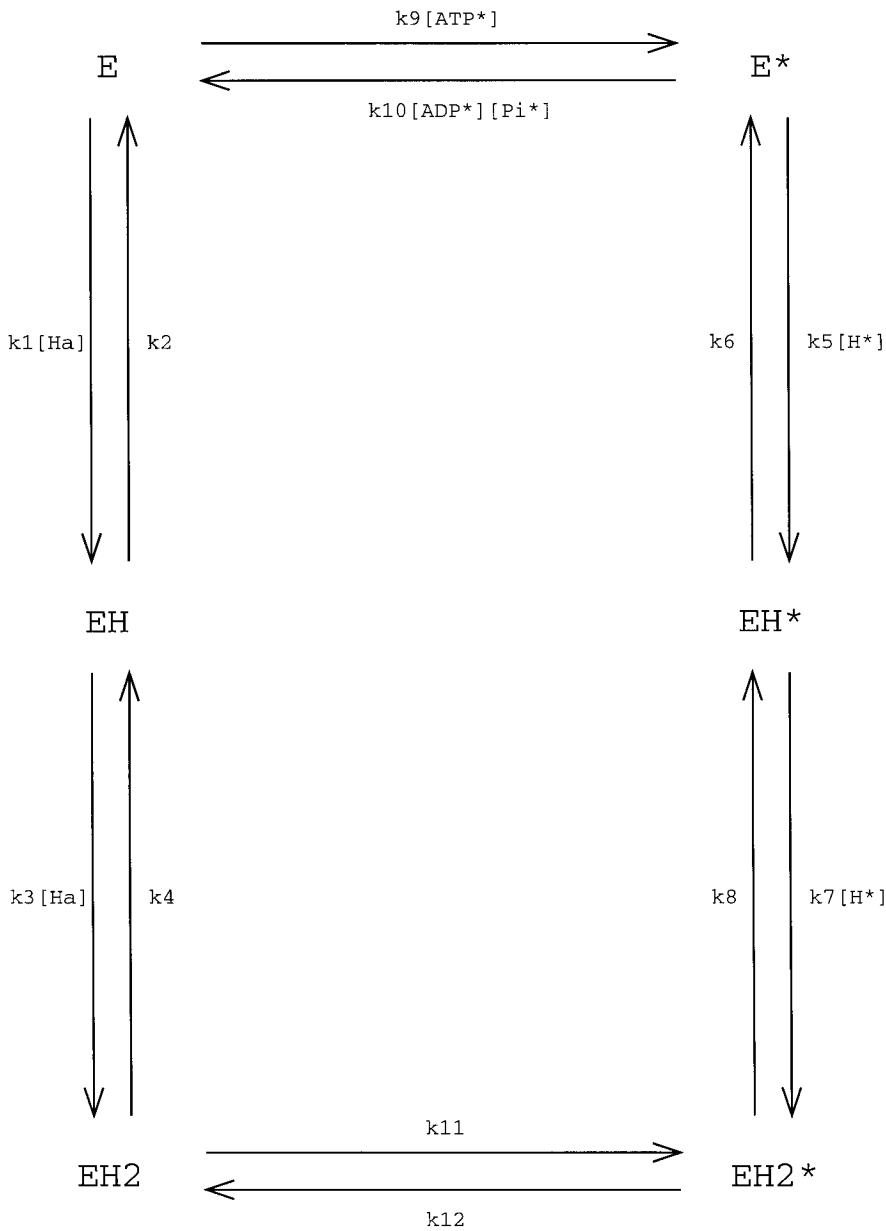


Fig. 5. State diagram of the catalytic unit of H-ATPase. The catalytic unit (E) has 2 binding sites for H. Symbols with asterisk (\*), such as EH\*, indicate conformations of the catalytic unit in which binding sites face the cytosolic space, and symbols without asterisk (e.g., EH) indicate conformations in which binding sites face the antechamber. Transition between the unloaded conformations (E→E\*) is coupled with ATP hydrolysis/synthesis. The label [H<sub>a</sub>] indicates H<sup>+</sup> concentration in the antechamber, and other bracketed labels, such as [ATP\*] and [H\*], indicate substrate concentrations in the cytosolic space. H<sup>+</sup> in the antechamber is assumed to be in equilibrium with extracellular H<sup>+</sup>, and electrical potential of the antechamber is assumed to be equal to that of cytosolic space. Therefore

$$[H_a] = [H]_o \exp \{F(\psi_o - \psi_i)/RT\}$$

where [H]<sub>o</sub> is extracellular H<sup>+</sup> concentration, and  $\psi_o$  and  $\psi_i$  are electrical potentials of the extracellular space and the intracellular space, respectively.

because A reflects the free energy difference ( $\Delta G$ ) between the unloaded inward- and outward-facing forms (E and E\*). A of the model exchanger is 0.18, which is within the range of experimental estimations (0.03–0.37; Refs. 36 and 49). Molar

Gibbs free energy change ( $\Delta G_m^0$ ) of the transition between the two unloaded forms is estimated from A ( $\Delta G_m^0 = -RT \log A$ ) to be 4.4 kJ/mol.

Table 2. Rate constants of H<sup>+</sup>-ATPase

$k_1$	$8.33 \times 10^9$	$\text{cm}^3 \cdot \text{mmol}^{-1} \cdot \text{s}^{-1}$
$k_2$	$1.00 \times 10^3$	$\text{s}^{-1}$
$k_3$	$8.33 \times 10^9$	$\text{cm}^3 \cdot \text{mmol}^{-1} \cdot \text{s}^{-1}$
$k_4$	$1.00 \times 10^4$	$\text{s}^{-1}$
$k_5$	$2.50 \times 10^{10}$	$\text{cm}^3 \cdot \text{mmol}^{-1} \cdot \text{s}^{-1}$
$k_6$	$1.00 \times 10^3$	$\text{s}^{-1}$
$k_7$	$2.50 \times 10^{10}$	$\text{cm}^3 \cdot \text{mmol}^{-1} \cdot \text{s}^{-1}$
$k_8$	$2.50 \times 10^2$	$\text{s}^{-1}$
$k_9$	$1.00 \times 10^9$	$\text{cm}^3 \cdot \text{mmol}^{-1} \cdot \text{s}^{-1}$
$k_{10}$	$1.80 \times 10^5$	$\text{cm}^6 \cdot \text{mmol}^{-2} \cdot \text{s}^{-1}$
$k_{11}$	$5.00 \times 10^2$	$\text{s}^{-1}$
$k_{12}$	$1.00 \times 10^2$	$\text{s}^{-1}$

Parameter assignment. Values of model parameters are listed in Table 4. Values directly related to acid-base transport are as follows. Permeabilities of NH<sub>3</sub> are 0.0113 cm/s and 0.0036 cm/s in the luminal and the basolateral membrane, respectively. These values are from the measurement in the rabbit cortical collecting duct (82). Permeability of H<sub>2</sub>CO<sub>3</sub> through luminal membranes is  $1.28 \times 10^{-3}$  cm/s, which is estimated from the apical membrane formic acid permeability ( $4.6 \times 10^{-2}$  cm/s; Ref. 68) in the rat proximal tubule and its 36-fold amplification of the luminal surface area by microvilli (52). Permeabilities of Cl<sup>-</sup> via basolateral conductances in type A and type B intercalated cells are  $7.40 \times 10^{-6}$  and  $1.80 \times 10^{-5}$  cm/s, respectively. These values are from the basolateral conductances of the intercalated cells in the model of cortical collecting duct by Strieter et al. (73).

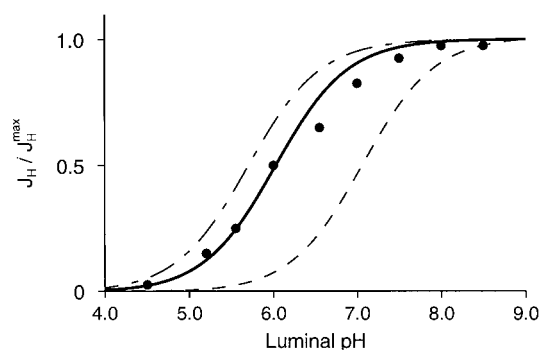


Fig. 6. Transport velocity of the model H-ATPase. Transport velocity of the model H-ATPase is plotted as a function of luminal pH. The solid continuous line is calculated with the conditions (cytosolic pH 7.5; luminal potential 0 mV; and cytosolic potential  $-30$  mV) that simulate experiments by Andersen et al. (3). Solid circles represent corresponding experimental values (3). Transport velocity is normalized by the transport velocity with luminal pH of 9.0 ( $J_H^{\max}$ ). The dashed line represents a calculation with the conditions simulating distal convoluted tubule cells (cytosolic pH 7.0; luminal potential 0 mV; and cytosolic potential  $-90$  mV). The dashed-dotted line represents a calculation with the conditions simulating type A intercalated cells (cytosolic pH 7.4; luminal potential  $-17$  mV; and cytosolic potential  $-26$  mV).  $J_H$ , rate of  $H^+$  transport via H-ATPase.

We have assumed that  $NH_4^+$  permeability through the paracellular pathway is the same as those of other cations, because no experimental information is available about its value. Similarly, permeability of  $HCO_3^-$  through the paracellular pathway ( $P_{HCO_3^-}^{ms}$ ) has been assumed to be equal to that of  $Cl^-$ . This value ( $2.40 \times 10^{-6}$  cm/s), however, is significantly smaller than the value reported by Chan et al. (20). They measured  $HCO_3^-$  backflux during the perfusion of the rat distal tubule with nominally  $HCO_3^-$ -free solution and deduced a  $P_{HCO_3^-}^{ms}$  value of  $2.32 \times 10^{-5}$  cm/s. However, this value is larger than the estimated paracellular  $HCO_3^-$  permeability of the rat proximal tubule ( $1.77 \times 10^{-5}$ ; Ref. 23), a "leaky" epithelium, and should be regarded, as they had pointed out (20), as the estimation of the upper limit of paracellular  $HCO_3^-$  permeability in the distal tubule, because processes not directly related to paracellular  $HCO_3^-$  entry, such as the diffusion of ammonia from blood into the tubule lumen, can affect the measurement of  $HCO_3^-$  backflux. Consequently, instead of adopting their value, we have assumed that paracellular  $HCO_3^-$  permeability is equal to that of  $Cl^-$ , which had been determined from the transepithelial conductance of the distal tubule (22, 63). If we recalculate the model predictions with a  $P_{HCO_3^-}^{ms}$  value of  $2.32 \times 10^{-5}$  cm/s,  $HCO_3^-$  reabsorption in the distal tubule decreases by 9.2 pmol/min in the basic state due to an increased backflux of  $HCO_3^-$  through the paracellular pathway.

The value of the rate constant of  $H_2CO_3$  hydrolysis in the luminal space ( $k_d^m$ ) has been chosen to be considerably larger than the value reported for carbonic anhydrase-free solution (35). This is based on the experiments by Malnic et al. (62), who showed that to explain the relationship among measurements of luminal pH, luminal  $HCO_3^-$  concentration, and magnitude of  $H^+$  secretion in the distal tubule,  $k_d^m$  should be from 2.4- to 64.1-fold higher than the value in the carbonic anhydrase-free solution. In this model, we have assumed that  $k_d^m$  as well as  $k_h^m$  is 10-fold larger than the corresponding values in carbonic anhydrase-free solution (35). The origin of this higher  $k_d^m$  is not known. An authoritative immunocytochemical study (15) did not detect the membrane-bound form carbonic anhydrase in the distal tubule. However, a recent

study has shown that carbonic anhydrase immunoreactivity is detected on apical membranes of type A intercalated cells in the rabbit distal tubule (72). Therefore, a modest increase in  $k_d^m$  in the distal tubule might be due to carbonic anhydrase activity in apical membranes of a restricted group of tubular cells.

Other parameters that are related to acid-base transport have been chosen to fit free-flow micropuncture experiments by Capasso et al. (16, 17): that is, a distal tubular  $HCO_3^-$  reabsorption rate of 53.2 pmol/min in normal rats<sup>7</sup> and 179 pmol/min in acutely bicarbonate-loaded rats. To find those values, we have employed an epithelial model, which neglects axial changes of solute concentrations and greatly simplifies model equations. After determining the parameters that are directly related to acid-base transport as above, we have redone the parameter optimization procedure that had been conducted in the previous study (22), using the Powell method, to fit the model with experimental data of  $Na^+$ ,  $K^+$ ,  $Cl^-$ , and water transport in the rat distal tubule.

## RESULTS

*Comparison with free-flow micropuncture experiments.* We first examine whether incorporation of the new cell types and transporters has not affected the goodness of fit of the previous model. Model predictions of transport of  $Na^+$ ,  $K^+$ ,  $Cl^-$ , and water and luminal electrical potentials in the basic state are listed in Table 5 (details of the boundary conditions are described in the legend). As in the previous model, they are consistent with free-flow micropuncture experiments in the following conditions: in the basic state, in the presence of thiazide, in the presence of amiloride, and under the high sodium load with increased flow rate. Thus the extensions that have been introduced in the present model preserve the goodness of fit of the previous model.

Acid-base transport in the model tubule is summarized in Table 6. The rate of  $HCO_3^-$  reabsorption is 62.4 pmol/min in the basic state. This value is comparable to the experimental estimation of 53.2 pmol/min (17). Both early and late subsegments contribute to this  $HCO_3^-$  reabsorption, with the early subsegment reabsorbing at 44.3 pmol/min and the late subsegment at 18.2 pmol/min. This is also comparable to the results of Wang et al. (76), in which  $HCO_3^-$  reabsorption rates were 32.9 pmol/min in the early subsegment and 13.9 pmol/min in the late subsegment.<sup>8</sup>

One of the benefits of modeling the renal tubule is that it allows for determination of transport velocities through all of the transporters (Figs. 1 and 2). On the basis of these velocities, we can quantitatively estimate the relative importance of each transport mechanism. In the case of  $HCO_3^-$  reabsorption, two separate mech-

<sup>7</sup>Actually, they reported that  $HCO_3^-$  concentrations of the distal tubular fluid were 9.8 and 9.2 mM at the inlet and the outlet, respectively. Using estimated tubular fluid flow rates (7.99 nl/min at the inlet and 2.73 nl/min at the outlet; Ref. 22), we have estimated  $HCO_3^-$  reabsorption rate to be  $9.8 \times 7.99 - 9.2 \times 2.73 = 53.2$  pmol/min.

<sup>8</sup>Reabsorption rates per unit length have been converted to total reabsorption rates, assuming the lengths of the early and the late portions to be 1 and 1.3 mm, respectively.

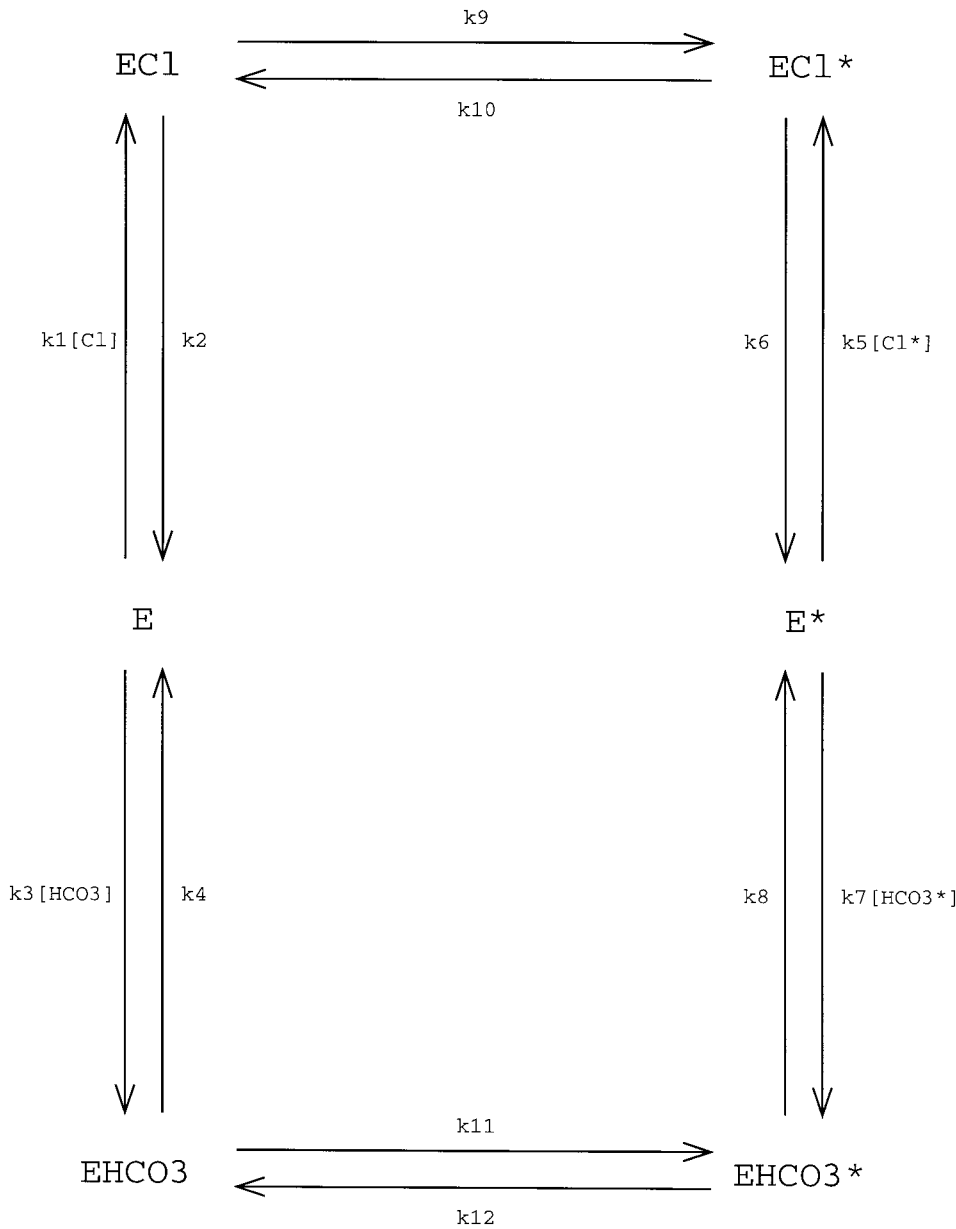


Fig. 7. State diagram of anion exchanger. The model transporter (E) has a single binding site to which  $Cl^-$  and  $HCO_3^-$  competitively bind. Only loaded transporters (EC1 and EHC03 in the extracellular side; and EC1\* and EHC03\* in the intracellular side) can cross the membrane. Brackets indicate substrate concentrations.

anisms can be involved: addition of  $H^+$  into the tubular fluid and transport of  $HCO_3^-$  itself out of the tubular fluid. The former mechanism can be divided further into secretion of  $H^+$  via luminal transporters and generation of  $H^+$  through chemical reactions. In the early distal tubule, the model shows that secretion of  $H^+$  is the major mechanism of  $HCO_3^-$  reabsorption (Table 6). In total,  $H^+$  is secreted at 48.0 pmol/min, in which 79% is ascribed to Na/H exchanger and 21% to H-ATPase. The magnitude of other components is much smaller: chemical generation of  $H^+$  is  $-1.1$  pmol/min (that is,  $H^+$  is consumed at 1.1 pmol/min), and  $HCO_3^-$  is secreted via the paracellular pathway at the rate of 2.6 pmol/min. With regard to the origin of secreted  $H^+$ , all of the ions are generated by chemical reactions in distal convoluted tubule cells: 97% from dissociation of carbonic acid ( $H_2CO_3 \rightarrow H^+ + HCO_3^-$ ) and 3% from disso-

ciation of ammonium ion ( $NH_4^+ \rightarrow H^+ + NH_3$ ). In the late distal tubule, luminal secretion of  $H^+$  becomes much smaller (15.2 pmol/min) due to the absence of luminal Na/H exchanger in this subsegment. On the other hand, amount of  $H^+$  generated by ammonium and phosphate buffer systems becomes larger (8.0 pmol/min in total).

Solute concentrations and electrical potentials in the basic state are listed in Tables 7 and 8. In the early distal tubule (Table 7), intracellular potential is highly hyperpolarized (on average,  $-89.8$  mV) and is consistent with experimental measurements (80). Intracellular  $Na^+$  concentration is low (on average, 9.5 mM), and intracellular  $K^+$  concentration is high (on average, 175 mM), reflecting the high Na-K-ATPase activity in these cells (22, 48). These values as well as the intracellular  $Cl^-$  concentration are consistent with the results of

Table 3. Rate constants of anion exchanger

$k_1$	$1.00 \times 10^8$	$\text{cm}^3 \cdot \text{mmol}^{-1} \cdot \text{s}^{-1}$
$k_2$	$7.87 \times 10^6$	$\text{s}^{-1}$
$k_3$	$1.00 \times 10^8$	$\text{cm}^3 \cdot \text{mmol}^{-1} \cdot \text{s}^{-1}$
$k_4$	$8.28 \times 10^6$	$\text{s}^{-1}$
$k_5$	$1.00 \times 10^8$	$\text{cm}^3 \cdot \text{mmol}^{-1} \cdot \text{s}^{-1}$
$k_6$	$7.87 \times 10^6$	$\text{s}^{-1}$
$k_7$	$1.00 \times 10^8$	$\text{cm}^3 \cdot \text{mmol}^{-1} \cdot \text{s}^{-1}$
$k_8$	$8.28 \times 10^6$	$\text{s}^{-1}$
$k_9$	$5.14 \times 10^5$	$\text{s}^{-1}$
$k_{10}$	$9.26 \times 10^4$	$\text{s}^{-1}$
$k_{11}$	$3.24 \times 10^5$	$\text{s}^{-1}$
$k_{12}$	$5.83 \times 10^4$	$\text{s}^{-1}$
$K_i^{\text{Cl}}$	0.528	$\text{mmol}/\text{cm}^3$
$K_i^{\text{HCO}_3}$	0.423	$\text{mmol}/\text{cm}^3$

In the present model of the anion exchanger, there is an internal modifier site (not shown in Fig. 7) that has dissociation constants of  $K_i^{\text{Cl}}$  and  $K_i^{\text{HCO}_3}$  for internal Cl and  $\text{HCO}_3^-$ , respectively. Occupancy of this site prohibits the anion exchanger from participating in ion transport. Therefore, net Cl influx ( $J_{\text{Cl}}^{\text{influx}}$ ) via a single anion exchanger is

$$J_{\text{Cl}}^{\text{influx}} = (k_9[\text{ECl}] - k_{10}[\text{ECl}^*]) \times \left(1 + \frac{[\text{Cl}^*]}{K_i^{\text{Cl}}} + \frac{[\text{HCO}_3^*]}{K_i^{\text{HCO}_3}}\right)^{-1}$$

where  $[\text{ECl}]$  and  $[\text{ECl}^*]$  are probability that the transporter is in each state at the steady state,  $[\text{Cl}^*]$  is intracellular  $\text{Cl}^-$  concentration, and  $[\text{HCO}_3^*]$  is intracellular  $\text{HCO}_3^-$  concentration.  $[\text{ECl}]$  and  $[\text{ECl}^*]$  are calculated by solving the state diagram as usual (using only  $k_1$ – $k_{12}$ ).

electron microprobe analysis on distal tubular cells (7). Mean intracellular pH is 6.94. Together with the luminal pH and potential difference, it can be calculated that  $\text{H}^+$  is secreted against the electrochemical gradient of 10.6 kJ/mol at the apical membrane of the distal convoluted tubule cells. This is accomplished via the Na/H exchanger by utilizing the electrochemical gradient of  $\text{Na}^+$  (11.3 kJ/mol) across the apical cell membrane and via H-ATPase by utilizing the free energy change of ATP hydrolysis (59 kJ/mol, coupled with transport of 2 mol of  $\text{H}^+$ ).

In the late distal tubule (Table 8), principal cells show intracellular potential and concentrations of  $\text{Na}^+$ ,  $\text{K}^+$ , and  $\text{Cl}^-$  that are consistent with experimental measurements (7, 80). Intracellular pH of principal cells is 6.59, which is determined mainly by the Na/H exchanger and the anion exchanger in the basolateral membrane and is not directly related to transepithelial acid-base transport. In intercalated cells, intracellular potentials are  $-26$  and  $-24$  mV for type A and type B intercalated cells, respectively. These values are consistent with experimental measurements (from  $-19$  to  $-26$  mV) with intercalated cells of the rabbit cortical collecting duct (34). Intracellular  $\text{Cl}^-$  concentrations are near the equilibrium values (with respect to the bath  $\text{Cl}^-$ ), which is due to the  $\text{Cl}^-$ -selective basolateral membrane of the intercalated cells (34, 50, 51, 64). Intracellular pH in the type A intercalated cells is 7.35; and  $\text{H}^+$  is secreted against the gradient of 4.25 kJ/mol across the apical membrane via H-ATPase.

The axial profile of luminal  $\text{HCO}_3^-$  concentration is plotted in the upper panel of Fig. 10. In the early distal tubule, luminal  $\text{HCO}_3^-$  concentration decreased steadily from its inlet value of 9.8–5.2 mM, whereas in the late distal tubule it increased again up to 9.3 mM and then

decreased to 6.6 mM. As a whole, this is compatible with the experimental observation that there was no fixed trend of change in luminal  $\text{HCO}_3^-$  concentration along the distal tubule (62). Apparently, the paradoxical increase in  $\text{HCO}_3^-$  concentration in the late segment, in the face of active  $\text{H}^+$  secretion, is ascribable to prominent water reabsorption in this part of nephron that concentrates tubular fluid (22). The axial profile of luminal pH is plotted in the middle panel of Fig. 10 (solid line). Values of luminal pH range from 6.47 to 6.84 (mean 6.69) and are comparable to experimental measurement (range 5.75–6.91; mean 6.35 in Ref. 62). The initial increase in luminal pH in the late distal tubule is, again, ascribable to water reabsorption. Concentrated tubular fluid tends to have higher levels of  $\text{HCO}_3^-$ ,  $\text{H}_2\text{CO}_3$ , and  $\text{CO}_2$ . However, permeability

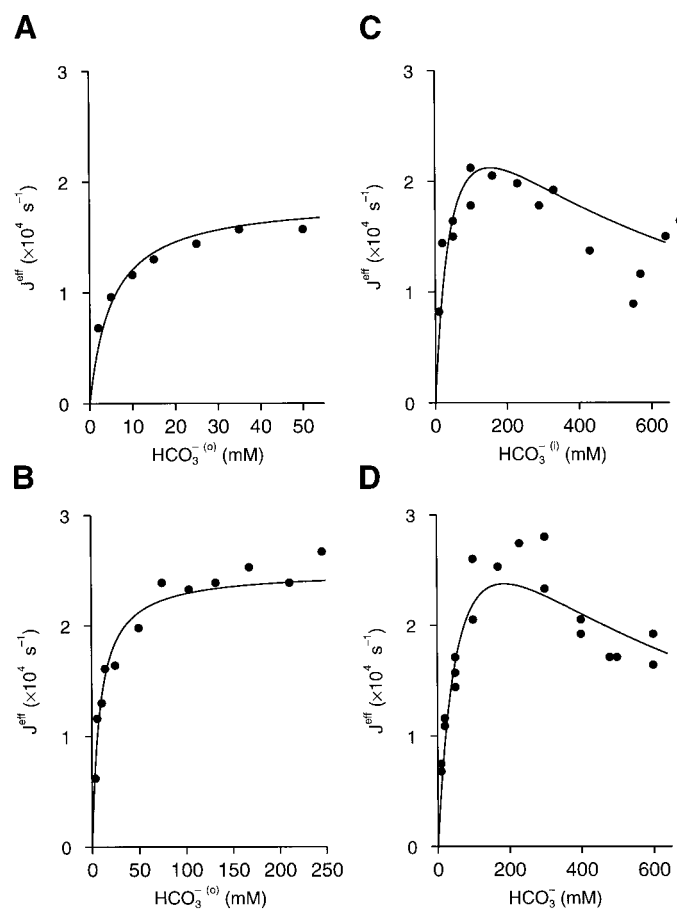


Fig. 8. Transport velocity of the model anion exchanger:  $\text{HCO}_3^-$  dependency. Transport velocity of the model anion exchanger is calculated as a function of  $\text{HCO}_3^-$  concentration and is plotted as a solid line. Experimental data (36) are plotted together as solid circles. A: unidirectional  $\text{HCO}_3^-$  efflux ( $J^{\text{eff}}$ ) as extracellular (o)  $\text{HCO}_3^-$  concentration is varied from 0 to 54 mM. Internal (i)  $\text{HCO}_3^-$  concentration is 50 mM. There are no  $\text{Cl}^-$  ions. B: unidirectional  $\text{HCO}_3^-$  efflux as extracellular  $\text{HCO}_3^-$  is varied from 0 to 250 mM. Internal  $\text{HCO}_3^-$  concentration is 165 mM. There are no  $\text{Cl}^-$  ions. C: unidirectional  $\text{HCO}_3^-$  efflux as internal  $\text{HCO}_3^-$  concentration is varied from 0 to 640 mM. External  $\text{HCO}_3^-$  concentration is 50 mM. There are no  $\text{Cl}^-$  ions. D:  $\text{HCO}_3^-$  exchange flux ( $J^{\text{eff}}$ ) as extracellular and intracellular  $\text{HCO}_3^-$  concentrations are varied simultaneously (no  $\text{HCO}_3^-$  gradient) from 0 to 640 mM. There are no  $\text{Cl}^-$  ions. Experimental data are from Fig. 5 in Ref. 36.

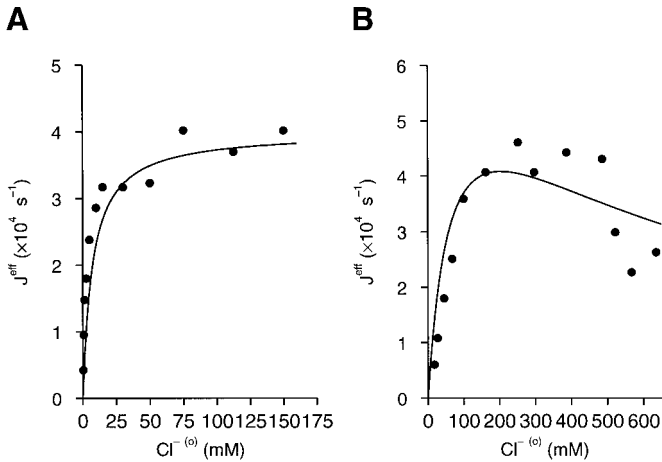


Fig. 9. Transport velocity of the model anion exchanger: Cl<sup>-</sup> dependency. Transport velocity of the model anion exchanger is calculated as a function of Cl<sup>-</sup> concentration and is plotted as a solid line. Experimental data (49) are plotted together as solid circles. A: unidirectional Cl<sup>-</sup> efflux as extracellular Cl<sup>-</sup> concentration is varied from 0 to 160 mM. Internal Cl<sup>-</sup> concentration is 105.4 mM. There are no HCO<sub>3</sub><sup>-</sup> ions. B: Cl<sup>-</sup> exchange flux as extracellular and intracellular Cl<sup>-</sup> concentrations are varied simultaneously (no Cl<sup>-</sup> gradient) from 0 to 650 mM. There are no HCO<sub>3</sub><sup>-</sup> ions. Experimental data are representative points of Figs. 1 and 4 in Ref. 49.

for CO<sub>2</sub> is so high that CO<sub>2</sub> diffuses out quickly and CO<sub>2</sub> concentration remains essentially unchanged. Consequently, the following chemical reaction is driven rightward: HCO<sub>3</sub><sup>-</sup> + H ⇌ H<sub>2</sub>CO<sub>3</sub> ⇌ CO<sub>2</sub> + H<sub>2</sub>O. Disequilibrium pH is represented in Fig. 10 (middle panel) as the difference between the solid line and the broken line. Disequilibrium pH is larger in the early distal tubule (range 0.23–0.30; mean 0.29) than in the late distal tubule (range 0.11–0.23; mean 0.14), reflecting the larger H<sup>+</sup> secretion rate in the former. These values are comparable to the level of disequilibrium pH observed in micropuncture experiments (for example, 0.37 in Ref. 62). The profile of HCO<sub>3</sub><sup>-</sup> reabsorption rate is plotted in the bottom panel of Fig. 10. When the early and late subsegments are compared, reabsorption rate in the early subsegment is larger than that in the late subsegment. However, within each subsegment, the HCO<sub>3</sub><sup>-</sup> reabsorption rate is relatively constant, which is in contrast to profiles of reabsorption rates of other solutes (22).

The axial profile of luminal NH<sub>4</sub><sup>+</sup>, NH<sub>3</sub>, and total phosphate (H<sub>2</sub>PO<sub>4</sub><sup>-</sup> + HPO<sub>4</sub><sup>2-</sup>) concentrations are plotted in Fig. 11. The luminal NH<sub>4</sub><sup>+</sup> concentration is 3.2 mM at the inlet, which is 47-fold higher than the basolateral NH<sub>4</sub><sup>+</sup> concentration. It is essentially constant in the early distal tubule. In the late distal tubule, it increases transiently up to 6.3 mM in the

Table 4. Model parameters

		DCT	P	A	B
$J_{TSC,max}^{mc}$	mmol·s <sup>-1</sup> ·cm <sup>-2</sup>	4.59 × 10 <sup>-5</sup>	4.59 × 10 <sup>-6</sup>		
$J_{NHE,max}^{mc}$	mmol·s <sup>-1</sup> ·cm <sup>-2</sup>	7.15 × 10 <sup>-5</sup>			
$J_{KCl,max}^{mc}$	mmol·s <sup>-1</sup> ·cm <sup>-2</sup>	3.48 × 10 <sup>-8</sup>	4.89 × 10 <sup>-7</sup>		
$J_{H-ATPase,max}^{mc}$	mmol·s <sup>-1</sup> ·cm <sup>-2</sup>	6.44 × 10 <sup>-7</sup>		2.94 × 10 <sup>-7</sup>	
$J_{AE,max}^{mc}$	mmol·s <sup>-1</sup> ·cm <sup>-2</sup>				1.81 × 10 <sup>-6</sup>
$P_{Na}^{mc}$	cm·s <sup>-1</sup>	2.63 × 10 <sup>-6</sup>	1.24 × 10 <sup>-5</sup>		
$P_{K}^{mc}$	cm·s <sup>-1</sup>	4.51 × 10 <sup>-7</sup>	3.66 × 10 <sup>-5</sup>		
$P_{Cl}^{mc}$	cm·s <sup>-1</sup>	2.24 × 10 <sup>-6</sup>	8.06 × 10 <sup>-6</sup>		
$P_{NH_4^+}^{mc}$	cm·s <sup>-1</sup>	9.01 × 10 <sup>-8</sup>	7.33 × 10 <sup>-6</sup>		
$P_{NH_3}^{mc}$	cm·s <sup>-1</sup>	1.13 × 10 <sup>-2</sup>	1.13 × 10 <sup>-2</sup>		
$P_{H_2CO_3}^{mc}$	cm·s <sup>-1</sup>	1.28 × 10 <sup>-3</sup>	1.28 × 10 <sup>-3</sup>		
$J_{a,max}^{sc}$	mmol·s <sup>-1</sup> ·cm <sup>-2</sup>	5.23 × 10 <sup>-6</sup>	1.64 × 10 <sup>-6</sup>		
$J_{H-ATPase,max}^{sc}$	mmol·s <sup>-1</sup> ·cm <sup>-2</sup>				5.96 × 10 <sup>-8</sup>
$J_{NHE,max}^{sc}$	mmol·s <sup>-1</sup> ·cm <sup>-2</sup>		3.09 × 10 <sup>-7</sup>		
$J_{AE,max}^{sc}$	mmol·s <sup>-1</sup> ·cm <sup>-2</sup>	4.19 × 10 <sup>-5</sup>	9.75 × 10 <sup>-6</sup>	1.89 × 10 <sup>-6</sup>	
$P_{K}^{sc}$	cm·s <sup>-1</sup>	5.29 × 10 <sup>-4</sup>	1.04 × 10 <sup>-4</sup>		
$P_{Cl}^{sc}$	cm·s <sup>-1</sup>	4.39 × 10 <sup>-5</sup>	1.20 × 10 <sup>-5</sup>	7.40 × 10 <sup>-6</sup>	1.80 × 10 <sup>-5</sup>
$P_{NH_4^+}^{sc}$	cm·s <sup>-1</sup>	1.06 × 10 <sup>-4</sup>	2.08 × 10 <sup>-5</sup>		
$P_{NH_3}^{sc}$	cm·s <sup>-1</sup>	3.60 × 10 <sup>-3</sup>	3.60 × 10 <sup>-3</sup>		
$P_{Na}^{ms}$	cm·s <sup>-1</sup>	4.80 × 10 <sup>-6</sup>	4.80 × 10 <sup>-6</sup>		
$P_{K}^{ms}$	cm·s <sup>-1</sup>	4.80 × 10 <sup>-6</sup>	4.80 × 10 <sup>-6</sup>		
$P_{NH_4^+}^{ms}$	cm·s <sup>-1</sup>	4.80 × 10 <sup>-6</sup>	4.80 × 10 <sup>-6</sup>		
$P_{Cl}^{ms}$	cm·s <sup>-1</sup>	2.40 × 10 <sup>-6</sup>	2.40 × 10 <sup>-6</sup>		
$P_{HCO_3^-}^{ms}$	cm·s <sup>-1</sup>	2.40 × 10 <sup>-6</sup>	2.40 × 10 <sup>-6</sup>		
$L_v^{mc}$	cm·s <sup>-1</sup> ·mmHg <sup>-1</sup>	5.22 × 10 <sup>-9</sup>	7.48 × 10 <sup>-8</sup>		
$L_v^{sc}$	cm·s <sup>-1</sup> ·mmHg <sup>-1</sup>	5.22 × 10 <sup>-7</sup>	7.48 × 10 <sup>-6</sup>	5.22 × 10 <sup>-8</sup>	5.22 × 10 <sup>-8</sup>
$z_{imp}^c$		-1.95	-1.57	0.348	0.266
$k_d^m$	s <sup>-1</sup>	496	496		
$k_h^m$	s <sup>-1</sup>	1.45	1.45		

DCT, distal convoluted cell; P, principal cell; A, type A intercalated cells; B, type B intercalated cells; mc, sc, and ms: luminal membrane, basolateral membrane, and tight junction, respectively;  $J_{x,max}$  stands for maximal transport velocity of transport mechanism x;  $J_{TSC,max}^{mc}$  maximal transport velocity of thiazide-sensitive Na-Cl cotransporter (TSC) in the luminal membrane; NHE, Na/H exchanger; a, Na-K-ATPase; AE, anion exchanger;  $P_x$ , permeability of ionic channel or membrane permeability, whereas x is the permeant molecule;  $L_v$ , hydraulic conductivity of the membrane;  $z_{imp}^c$  stands for valence of impermeant molecule in cytosolic space;  $k_d^m$  and  $k_h^m$ , rate constant of carbonic acid dehydration and hydration in the luminal space, respectively. Values of  $k_d^m$  and  $k_h^m$  in the present model are 10-fold larger than the values reported by Garg and Maren (35) in carbonic anhydrase-free solution. See METHODS for details.

Table 5. Basic transport characteristics

	Model	Experiment
<i>Basic State</i>		
$J_v$ , nl/min	5.47	5.26
$J_{Na}$ , pmol/min	367	340
$J_K$ , pmol/min	-22.4	-22.3
$\psi_{DCT}^m$ , mV	-2.2	-4.7
$\psi_{ICT}^m$ , mV	-20.2	-28.0
<i>Thiazide</i>		
$J_{Na}$ , pmol/min	254	192
$\psi_{DCT}^m$ , mV	-6.2	-4.7
$\psi_{ICT}^m$ , mV	-27.9	-28.0
<i>Amiloride</i>		
$J_{Na}$ , pmol/min	349	340
$\psi_{DCT}^m$ , mV	+5.5	-3.2
$\psi_{ICT}^m$ , mV	-6.1	-7.5
<i>High Load</i>		
$J_{Na}$ , pmol/min	681	732
$J_K$ , pmol/min	-99.4	-94.0

Model predictions have been calculated as in the previous study (22).  $J_v$ , transepithelial reabsorption of water;  $J_{Na}$ , transepithelial reabsorption of  $Na^+$ ;  $J_K$ , transepithelial reabsorption of  $K^+$ ;  $\psi_{DCT}^m$ , electrical potential at the middle of the early distal tubule;  $\psi_{ICT}^m$ , electrical potential at the middle of the late distal tubule. In the basic state, initial tubular fluid contains (in mM) 51.1  $Na^+$ , 1.86  $K^+$ , 45.1  $Cl^-$ , 9.8  $HCO_3^-$ , pH 6.71, 1.10  $H_2PO_4^-$ , 0.90  $HPO_4^{2-}$ , 3.17  $NH_4^+$ , and 73 urea, as well as 15.2  $\mu M NH_3$ , at a flow rate 8 nl/min. Thiazide application is simulated by reducing the maximal transport rate of the Na-Cl cotransporter by 90%. Amiloride application is simulated by reducing the permeability of the  $Na^+$  channel by 99%. State of high (volume and  $Na^+$ ) load is simulated by increasing the flow rate to 35 nl/min. In all the calculations, the bath solution consists of (in mM) 143.8  $Na^+$ , 4.25  $K^+$ , 112  $Cl^-$ , 24  $HCO_3^-$  (pH 7.4), and 20.88 impermeant molecule (with valence of -0.580) as well as 68.4  $\mu M NH_4^+$  and 1.60  $\mu M NH_3$  and has an electrical potential of 0 mV.

first half, which is the consequence of volume reabsorption. In the second half of the late distal tubule, luminal  $NH_4^+$  concentration decreases again, and it becomes 3.5 mM at the end of the distal tubule. This decrease is due to chemical conversion to  $NH_3$ , reabsorption via luminal  $NH_4^+$  conductance, and reabsorption via the paracellular pathway. The axial profile of the luminal  $NH_3$  concentration is similar to that of luminal  $NH_4^+$  concentration. This reflects the profile of luminal pH that shows only modest changes along the tubular axis. In total, ammonium (including both  $NH_4^+$  and  $NH_3$ ) is reabsorbed at the rate of 17 pmol/min in the distal tubule. This appears to be inconsistent with micropuncture experiments that show no significant ammonium reabsorption in the rat distal tubule (39, 44, 47). Possible reasons for this inconsistency are the following. First, direct measurement of  $NH_3$  permeability in the rat distal tubule is not available. We have assumed that it is similar to that in the rabbit<sup>9</sup> cortical

<sup>9</sup>In the rat (32), reported  $NH_3$  permeability in microperfused cortical collecting duct (0.024 cm/s) is one order of magnitude larger than that in the rabbit. If we adopt this value, with similar apical-to-basolateral permeability ratio as reported by Yip and Kurtz (82), total ammonium reabsorption becomes 24.1 pmol/min (95% of the inlet load).

collecting duct (82), but actual permeability in the rat distal tubule in vivo might be smaller. Second, we have assumed that  $NH_4^+$  permeability via K channel is 20% of  $K^+$  permeability on the basis of the data of single-channel conductances and mean open probabilities (66). However,  $K^+$ -to- $NH_4^+$  permeability ratio estimated from the difference in reversal potentials is  $\sim 10$  (66). Therefore, actual  $NH_4^+$  permeability in the distal tubule may be smaller than our estimation, resulting in smaller  $NH_4^+$  reabsorption rate. Third, ammonia production by metabolism is not incorporated in the present model. According to Good and Burg (42), the rate of ammonia production in the distal tubule is comparable to the proximal tubule (in terms of production per unit length) and is 5.5–6.7 pmol·min<sup>-1</sup>·mm<sup>-1</sup>. Assuming the total length of 2.3 mm, these values are translated to 13–15 pmol/min. If the fraction of ammonia thus produced is secreted into the tubular fluid, it would have the effect of reducing the net reabsorption rate of total ammonia. The axial profile of total phosphate concentration in the luminal compartment is strictly determined by the profile of water reabsorption, because phosphates are assumed to be impermeable in this model. A steeper change in total phosphate concentration implies greater water reabsorption. Inspection of Fig. 11 shows that water reabsorption is essentially confined in the first half of the late distal tubule.

Distal  $HCO_3^-$  reabsorption under high  $HCO_3^-$  load has been studied by Capasso et al. (16). They infused intravenously a solution containing 260 mM  $HCO_3^-$ , which brought about an approximately sixfold increase

Table 6. Acid-base transport characteristics

	$J_{HCO_3}$ (Base), pmol/min	$J_{HCO_3}$ (Bicarbonate Load), pmol/min
Total	62.4	217.7
DCT	44.3	140.1
- $J_H$ (NHE)	38.1	101.6
- $J_H$ (H-ATPase)	9.9	18.3
$J_{HCO_3}$ (paracellular)	-2.6	5.8
$G_{NH_3}$	0.7	17.2
$G_{HPO_4}$	-1.8	-2.8
ICT	18.2	77.5
- $J_H$ (H-ATPase)	15.2	13.7
$J_{HCO_3}$ (AE)	-3.6	-1.2
$J_{HCO_3}$ (paracellular)	-1.4	37.9
$G_{NH_3}$	5.2	22.2
$G_{HPO_4}$	2.8	4.9

Net  $HCO_3^-$  reabsorption ( $J_{HCO_3}$ ) in the basic state has been calculated with the same conditions as listed in Table 5. -  $J_H$  (NHE),  $H^+$  secretion through luminal Na/H exchanger (NHE); -  $J_H$  (H-ATPase),  $H^+$  secretion through luminal H-ATPase;  $J_{HCO_3}$  (paracellular),  $HCO_3^-$  reabsorption through paracellular pathway;  $J_{HCO_3}$  (AE),  $HCO_3^-$  secretion through luminal anion exchanger of type B intercalated cells;  $G_{NH_3}$ , rate of  $H^+$  generation due to chemical reaction of  $NH_4^+ \rightarrow H^+ + NH_3$ ; and  $G_{HPO_4}$ , rate of  $H^+$  generation due to chemical reaction of  $H_2PO_4^- \rightarrow H^+ + HPO_4^{2-}$ . Net  $HCO_3^-$  reabsorption during the bicarbonate load has been calculated according to the following conditions (16): initial tubular fluid comprising (in mM) 101  $Na^+$ , 1.86  $K^+$ , 43.16  $Cl^-$ , 55.7  $HCO_3^-$ , pH 7.47, 3.11  $NH_4^+$ , 0.08  $NH_3$ , 0.36  $H_2PO_4^-$ , 1.64  $HPO_4^{2-}$ , and 10 urea; flow rate of 8.64 nl/min; and the bath solution comprising (in mM) 144  $Na^+$ , 4.25  $K^+$ , 97.5  $Cl^-$ , and 38.5  $HCO_3^-$ , pH 7.61.

Table 7. *Solute concentrations and electrical potentials in the early distal tubule (basic state)*

	Mucosal	DCT Cell	Serosal
Electrical potential, mV	-1.60 (-9.50 ~ +5.62)	-89.8 (-95.8 ~ -82.2)	0.00
Na <sup>+</sup> , mM	27.9 (14.0 ~ 48.0)	9.45 (6.98 ~ 12.6)	143.8
K <sup>+</sup> , mM	2.13 (1.89 ~ 2.38)	175.4 (163.0 ~ 184.3)	4.25
Cl <sup>-</sup> , mM	24.8 (13.4 ~ 42.2)	35.7 (17.6 ~ 60.7)	112.0
pH	6.59 (6.47 ~ 6.70)	6.94 (6.68 ~ 7.18)	7.40
HCO <sub>3</sub> <sup>-</sup> , mM	7.38 (5.23 ~ 9.56)	8.83 (4.56 ~ 14.6)	24.0
H <sub>2</sub> CO <sub>3</sub> , μM	7.00 (6.65 ~ 7.13)	3.55 (3.55 ~ 3.55)	3.55
NH <sub>4</sub> <sup>+</sup> , mM	3.26 (3.18 ~ 3.37)	1.39 (0.93 ~ 1.98)	0.0684
NH <sub>3</sub> , μM	11.8 (9.19 ~ 14.9)	10.9 (8.82 ~ 13.2)	1.60
H <sub>2</sub> PO <sub>4</sub> <sup>-</sup> , mM	1.33 (1.12 ~ 1.57)		
HPO <sub>4</sub> <sup>2-</sup> , mM	0.81 (0.73 ~ 0.89)		
Urea, mM	78.2 (73.4 ~ 84.0)		
Impermeant solute, mM		72.7 (51.9 ~ 87.7)	20.9

Values are expressed as means (minimal value ~ maximal value) and are from the same calculation described in detail as the basic state in the legend for Table 5.

in HCO<sub>3</sub><sup>-</sup> load to the distal tubule (480 pmol/min). In this condition, they observed that HCO<sub>3</sub><sup>-</sup> reabsorption is markedly increased to the level of 179 pmol/min (control state: 53.2 pmol/min). When this experiment is

simulated by altering the boundary conditions (Table 6; boundary conditions are described in the legend), the model predicts a similar enhancement of HCO<sub>3</sub><sup>-</sup> reabsorption, amounting to 217.7 pmol/min. Both the early

Table 8. *Solute concentrations and electrical potentials in the late distal tubule (basic state)*

	Mucosal	P	A	B	Serosal
Electrical potential, mV	-17.3 (-20.3 ~ -3.64)	-86.5 (-92.7 ~ -85.0)	-25.7 (-26.0 ~ -24.5)	-24.2 (-25.5 ~ -23.4)	0.00
Na <sup>+</sup> , mM	20.1 (14.7 ~ 24.6)	9.31 (8.38 ~ 10.1)			143.8
K <sup>+</sup> , mM	11.2 (3.00 ~ 14.8)	166.3 (163.3 ~ 169.4)			4.25
Cl <sup>-</sup> , mM	24.8 (14.5 ~ 28.5)	15.6 (9.17 ~ 18.2)	57.4 (57.2 ~ 58.1)	46.8 (44.5 ~ 48.1)	112.0
pH	6.77 (6.54 ~ 6.84)	6.59 (6.41 ~ 6.64)	7.35 (7.34 ~ 7.35)	7.26 (7.22 ~ 7.31)	7.40
HCO <sub>3</sub> <sup>-</sup> , mM	7.84 (5.53 ~ 9.25)	3.75 (2.47 ~ 4.22)	21.4 (20.7 ~ 21.6)	17.2 (15.9 ~ 19.5)	24.0
H <sub>2</sub> CO <sub>3</sub> , μM	4.93 (4.51 ~ 5.97)	3.55 (3.55 ~ 3.55)	3.55 (3.55 ~ 3.55)	3.55 (3.55 ~ 3.55)	0.00
NH <sub>4</sub> <sup>+</sup> , mM	4.90 (3.46 ~ 6.25)	6.12 (4.16 ~ 7.83)			0.0684
NH <sub>3</sub> , μM	27.8 (12.1 ~ 40.0)	22.7 (11.9 ~ 32.1)			1.60
H <sub>2</sub> PO <sub>4</sub> <sup>-</sup> , mM	2.76 (1.71 ~ 3.37)				
HPO <sub>4</sub> <sup>2-</sup> , mM	2.65 (0.93 ~ 3.09)				
Urea, mM	197.1 (96.3 ~ 231.0)				
Impermeant solute, mM		103.5 (101.3 ~ 109.1)	226.2 (226.2 ~ 226.2)	241.0 (241.0 ~ 241.0)	20.9

Values are expressed as means (minimal value ~ maximal value) and are from the same calculation described in detail as the basic state in the legend for Table 5.

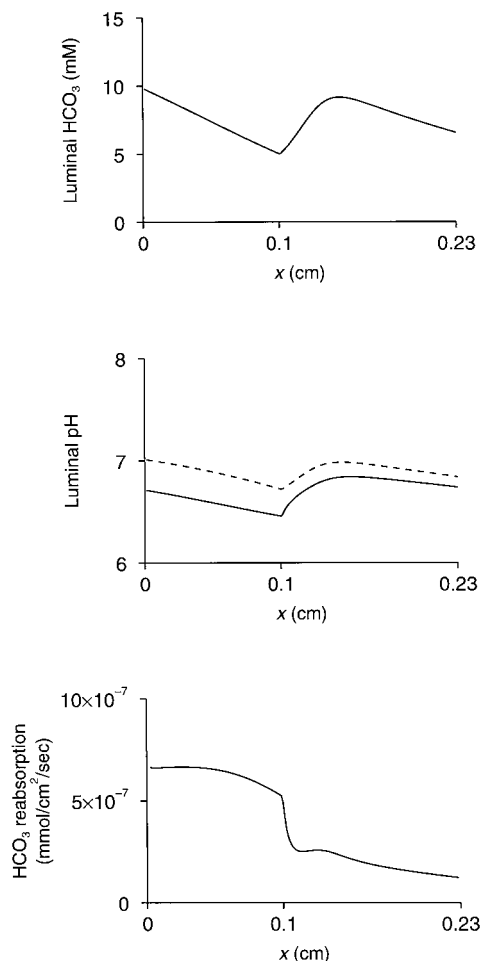


Fig. 10. Profiles of luminal  $\text{HCO}_3^-$  concentration, luminal pH, and  $\text{HCO}_3^-$  reabsorption rate along the tubular axis. *Top*: profile of luminal  $\text{HCO}_3^-$  concentration. *Middle*: profile of luminal pH (solid line). To illustrate disequilibrium pH, equilibrium pH (dashed line) is plotted together. The difference between the 2 lines indicates the magnitude of disequilibrium pH. *Bottom*: profile of transepithelial  $\text{HCO}_3^-$  reabsorption rate. The  $x$ -axis indicates the coordinate along tubular axis, with  $x = 0.1$  cm corresponding to the junction between early and late distal tubules. The figure was made from calculations with section width of 0.00125 cm.

and the late distal tubules contribute to this increase in  $\text{HCO}_3^-$  reabsorption. In the early distal tubule, the  $\text{HCO}_3^-$  reabsorption rate increases from 44.3 pmol/min in the basic state to 140.1 pmol/min under the bicarbonate load. Inspection of Table 6 reveals that this increase is largely due to the increase in  $\text{H}^+$  secretion via the luminal Na/H exchanger. From the solute concentrations and electrical potentials under the bicarbonate load that are listed in Table 9, we can see that the increased level of luminal  $\text{Na}^+$  (72.6 mM) is the cause of the increased Na/H exchanger activity. In the late distal tubule,  $\text{HCO}_3^-$  reabsorption rate is increased from 18.2 pmol/min in the basic state to 77.5 pmol/min under the bicarbonate load. From Table 6, it is evident that this change is mostly due to the increase in  $\text{HCO}_3^-$  reabsorption via the paracellular pathway. From the values of solute concentrations and electrical potentials (Table 10), we can see that more hyperpolarized

luminal potential ( $-40.8$  mV) and higher level of luminal  $\text{HCO}_3^-$  (95.9 mM) are responsible for the increased  $\text{HCO}_3^-$  current.

*Comparison with microperfusion experiments.* There are many microfusion experiments that examined  $\text{HCO}_3^-$  reabsorption in the rat distal tubule. In Table 11, we have listed them in two groups: those addressing the effect of perfusate  $\text{HCO}_3^-$  concentration on  $\text{HCO}_3^-$  reabsorption rate (*top*) and those addressing the effect of tubular flow rate (*bottom*). In the former group,  $\text{HCO}_3^-$  reabsorption rates were highly variable both in direction and in magnitude (Table 11). For example, with perfusate  $\text{HCO}_3^-$  concentration of  $\sim 10$  mM, Iacovitti et al. (46) reported net  $\text{HCO}_3^-$  secretion of  $12 \text{ pmol} \cdot \text{min}^{-1} \cdot \text{mm}^{-1}$ , whereas Chan et al. (20) reported net  $\text{HCO}_3^-$  reabsorption of  $26.1 \text{ pmol} \cdot \text{min}^{-1} \cdot \text{mm}^{-1}$ , which is comparable to micropuncture experiments ( $23.1 \text{ pmol} \cdot \text{min}^{-1} \cdot \text{mm}^{-1}$ ). With a similar boundary condition (described in the legend for Table 11), the model predicts net reabsorption of  $31.9 \text{ pmol} \cdot \text{min}^{-1} \cdot \text{mm}^{-1}$ , which is consistent with the experiment of Chan et al.

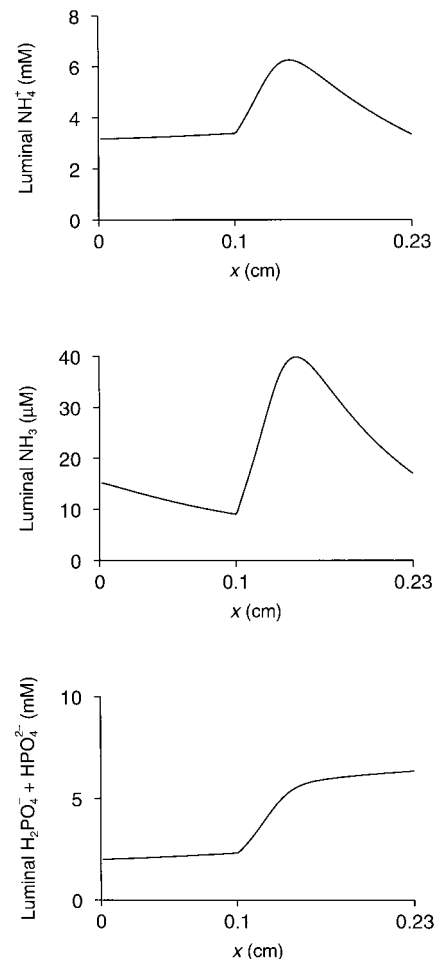


Fig. 11. Profiles of luminal  $\text{NH}_4^+$ ,  $\text{NH}_3$ , and phosphate ( $\text{H}_2\text{PO}_4^- + \text{HPO}_4^{2-}$ ) concentrations along the tubular axis. *Top*: profile of luminal  $\text{NH}_4^+$  concentration. *Middle*: profile of luminal  $\text{NH}_3$  concentration. *Bottom*: profile of luminal concentration of phosphates (sum of  $\text{H}_2\text{PO}_4^-$  and  $\text{HPO}_4^{2-}$ ). The figure was made from calculations with a section width of 0.00125 cm.

Table 9. Solute concentrations and electrical potentials in the early distal tubule (bicarbonate load)

	Mucosal	DCT Cell	Serosal
Electrical potential, mV	-12.8 (-19.0~-7.33)	-84.1 (-91.1~-75.6)	0.00
Na <sup>+</sup> , mM	72.6 (54.3~97.3)	11.6 (8.82~15.4)	143.8
K <sup>+</sup> , mM	2.14 (1.89~2.42)	163.5 (147.0~176.1)	4.25
Cl <sup>-</sup> , mM	19.3 (6.64~39.9)	51.5 (29.1~80.6)	97.5
pH	7.17 (7.01~7.35)	7.41 (7.24~7.58)	7.61
HCO <sub>3</sub> <sup>-</sup> , mM	51.2 (45.6~55.4)	25.2 (16.5~36.5)	38.5
H <sub>2</sub> CO <sub>3</sub> , μM	13.0 (9.23~16.6)	3.55 (3.55~3.55)	3.55
NH <sub>4</sub> <sup>+</sup> , mM	3.04 (3.01~3.10)	0.86 (0.83~0.91)	0.0684
NH <sub>3</sub> , μM	43.4 (29.2~64.6)	21.0 (14.7~31.6)	1.60
H <sub>2</sub> PO <sub>4</sub> <sup>-</sup> , mM	0.64 (0.44~0.86)		
HPO <sub>4</sub> <sup>2-</sup> , mM	1.47 (1.39~1.57)		
Urea, mM	10.6 (10.0~11.2)		
Impermeant solute, mM		50.9 (23.7~71.9)	21.0

Values are expressed as means (minimal value~maximal value) and are from the same calculation described in detail as the bicarbonate load in the legend for Table 6.

We tried to simulate the net HCO<sub>3</sub><sup>-</sup> secretion, as observed by Iacovitti et al. (46), by adjusting model parameters. When we modified single model parameter separately (keeping the other parameters constant), all attempts were unsuccessful. This suggests that changes restricted in single transport mechanism are not sufficient to account for the variation in microperfusion experiments. However, when all the activities in type B intercalated cells are increased, we have been able to reproduce net HCO<sub>3</sub><sup>-</sup> secretion. Specifically, if parameters related to all the transporters in type B intercalated cells (H-ATPase, anion exchanger, and Cl<sup>-</sup> channel) have been increased simultaneously by a factor of 30, the model has come to predict net HCO<sub>3</sub><sup>-</sup> secretion of 11.1 pmol·min<sup>-1</sup>·mm<sup>-1</sup>. We have thought such manipulation to be worth consideration, because it has been suggested that apparently inconsistent results in microperfusion experiments might be due to the different ways of feeding the experimental animals (54, 57). Such difference can affect the acid-base status of these animals and alter the activity of intercalated cells (71).

When perfusate HCO<sub>3</sub><sup>-</sup> concentration was increased to ~25 mM (Table 11), all investigators had reported a higher HCO<sub>3</sub><sup>-</sup> reabsorption rate. The actual magnitude, however, was again highly variable, ranging from 6 to 75.9 pmol·min<sup>-1</sup>·mm<sup>-1</sup> (20, 57). The model prediction (74.2 pmol·min<sup>-1</sup>·mm<sup>-1</sup>) agrees with the experiments that reported the highest reabsorption rate (20). We could not fit the model to experiments with low HCO<sub>3</sub><sup>-</sup> reabsorption rates, either by adjusting individual model parameters or by increasing the activity of type B intercalated cells.

Before we proceed to the effect of flow rate (Table 11), we compare the model with an experiment that separately perfused early and late distal tubules with normal flow rate (76). Varying the perfusate HCO<sub>3</sub><sup>-</sup> concentrations, Wang et al. (76) observed positive correlations between perfusate HCO<sub>3</sub><sup>-</sup> concentration and HCO<sub>3</sub><sup>-</sup> reabsorption rate both in the early distal tubule (Fig. 12A, ●) and in the late distal tubule (Fig. 12B). The present model also predicts a higher HCO<sub>3</sub><sup>-</sup> reabsorption rate as the perfusate HCO<sub>3</sub><sup>-</sup> is raised (solid lines<sup>10</sup> in Fig. 12). However, quantitative agreement is poor, especially in the late distal tubule. This may suggest that 1) our formulation of transporter kinetics (e.g., HCO<sub>3</sub><sup>-</sup> conductance in the tight junction) is inadequate in the case of unphysiologically high HCO<sub>3</sub><sup>-</sup> concentration in the tubular fluid; or 2) a transport mechanism exists that is not incorporated in the present model, but its transport rate is not negligible with a very high luminal HCO<sub>3</sub><sup>-</sup> concentration.

When the flow rate was increased from a lower range (5–10 nl/min) to a higher range (20–30 nl/min), microperfusion experiments revealed an increased (20, 57), unchanged (20, 57), or decreased (46, 56, 57) HCO<sub>3</sub><sup>-</sup> reabsorption rate (Table 11). The model predicts only small changes in HCO<sub>3</sub><sup>-</sup> reabsorption rate as flow rate is increased (Table 11). The flow-dependent in-

<sup>10</sup>Deflections in HCO<sub>3</sub><sup>-</sup> reabsorption rate observable at the perfusate HCO<sub>3</sub><sup>-</sup> concentration of 50–60 mM are probably due to the abrupt change in the perfusate Na<sup>+</sup> concentration between the lower HCO<sub>3</sub><sup>-</sup> experiments (70 mM Na<sup>+</sup>, when HCO<sub>3</sub><sup>-</sup> ≤50 mM) and the higher HCO<sub>3</sub><sup>-</sup> experiments (146 mM Na<sup>+</sup>, when HCO<sub>3</sub><sup>-</sup> ≥60 mM). See the legend for Fig. 12 for details.

Table 10. Solute concentrations and electrical potentials in the late distal tubule (bicarbonate load)

	Mucosal	P	A	B	Serosal
Electrical potential, mV	-40.8 (-46.8 ~ -25.2)	-81.4 (-89.6 ~ -79.5)	-26.0 (-26.0 ~ -25.8)	-79.3 (-93.9 ~ -70.5)	0.00
Na <sup>+</sup> , mM	99.3 (58.7 ~ 113.2)	14.4 (12.2 ~ 16.1)			143.8
K <sup>+</sup> , mM	24.6 (3.36 ~ 42.3)	158.9 (149.8 ~ 168.0)			4.25
Cl <sup>-</sup> , mM	9.33 (6.19 ~ 12.1)	17.7 (10.7 ~ 21.5)	50.0 (50.0 ~ 50.1)	5.47 (3.09 ~ 7.26)	97.5
pH	7.75 (7.18 ~ 7.96)	6.89 (6.70 ~ 6.99)	7.48 (7.48 ~ 7.48)	7.79 (7.77 ~ 7.80)	7.61
HCO <sub>3</sub> <sup>-</sup> , mM	95.9 (49.9 ~ 109.6)	7.63 (4.75 ~ 9.29)	28.8 (28.7 ~ 28.8)	58.5 (56.8 ~ 60.9)	38.5
H <sub>2</sub> CO <sub>3</sub> , μM	6.39 (4.43 ~ 12.3)	3.55 (3.55 ~ 3.55)	3.55 (3.55 ~ 3.55)	3.55 (3.55 ~ 3.55)	0.00
NH <sub>4</sub> <sup>+</sup> , mM	1.84 (0.06 ~ 4.01)	7.07 (0.67 ~ 14.6)			0.0684
NH <sub>3</sub> , μM	76.8 (5.10 ~ 167.0)	54.8 (4.12 ~ 120.0)			1.60
H <sub>2</sub> PO <sub>4</sub> <sup>-</sup> , mM	0.54 (0.46 ~ 0.75)				
HPO <sub>4</sub> <sup>2-</sup> , mM	5.09 (1.79 ~ 6.66)				
Urea, mM	28.1 (12.7 ~ 35.6)				
Impermeant solute, mM		98.9 (94.8 ~ 106.1)	226.2 (226.2 ~ 226.2)	241.1 (241.1 ~ 241.1)	21.0

Values are expressed as means (minimal value ~ maximal value) and are from the same calculation described in detail as the bicarbonate load in the legend for Table 6.

crease in HCO<sub>3</sub><sup>-</sup> reabsorption rate in several experiments could not be simulated by adjusting model parameters. The flow-dependent decrease, however, can be simulated by increasing the activity of type B intercalated cells. By increasing the transporter activities of type B intercalated cell by 30-fold, the model tubule shows an HCO<sub>3</sub><sup>-</sup> reabsorption rate of -11.1, -20.6, and -28.9 pmol·min<sup>-1</sup>·mm<sup>-1</sup> for flow rates of 8, 12, and 24 nl/min, respectively (perfusate HCO<sub>3</sub><sup>-</sup> concentration is 10 mM; for other boundary conditions, see the legend for Table 11).

## DISCUSSION

We have developed a numerical model to simulate acid-base transport in the rat distal tubule. The model is based on our previous model that dealt with Na<sup>+</sup>, K<sup>+</sup>, Cl<sup>-</sup>, and water transport in this nephron segment (22). Modifications have included incorporation of buffer systems, intercalated cells, and relevant transporters and adaptation of model equations to molecular interconversion in buffer systems and establishment of disequilibrium pH due to H<sup>+</sup> secretion. The extended model has simulated the results of micropuncture experiments addressing the transepithelial HCO<sub>3</sub><sup>-</sup> reabsorption both in the normal state and under the bicarbonate load. The model has also simulated the results of a set of in vivo microperfusion experiments.

*Experimental evidence supporting the selection of transporters.* There is pharmacological evidence for the existence of an Na/H exchanger in the luminal membrane of the early distal tubule. For example, Wang et

al. (76) reported that luminal application of ethylisopropylamiloride (EIPA; an inhibitor of the Na/H exchanger) reduced HCO<sub>3</sub><sup>-</sup> reabsorption by 65% in the early distal tubule, whereas it did not affect HCO<sub>3</sub><sup>-</sup> reabsorption in the late distal tubule. Claveau et al. (25) also demonstrated EIPA-sensitive Na<sup>+</sup> uptake in the luminal membrane vesicles prepared from rabbit distal tubules. They further suggested, based on pharmacological characteristics, that this Na/H exchange activity is mediated by the type 1 Na/H exchanger isoform (NHE1) among the six isoforms of Na/H exchanger (NHE1-NHE6) (65). Unfortunately, this suggestion is not supported by histological studies (9), and the identification of the isoform remains controversial (11, 18, 19, 67). However, investigators appear to agree on the point that NHE3 is not the major isoform in the distal tubule (2, 10). In the present model, the kinetic model of the Na/H exchanger has been constructed to fit the kinetics of the NHE3 isoform, because this is the most extensively studied isoform (5, 77). Therefore, it may be argued that this kinetic model is inadequate to represent the Na/H exchanger in the distal tubule because of the possible heterogeneity in transport kinetics of the individual isoforms. In actuality, however, such heterogeneity appears to be small. According to a study that compared basic kinetics of NHE1, NHE2, and NHE3 isoforms (58), affinity for external Na<sup>+</sup> and cooperativity of internal H<sup>+</sup> (in the internal modifier site) are similar among these isoforms. Hence, usage of kinetics of NHE3 isoform in the present model would be justified.

Table 11. *In vivo* microperfusion experiments vs. model predictions: dependence of net  $\text{HCO}_3^-$  reabsorption on perfusate  $\text{HCO}_3^-$  concentration and flow rate

$J_{\text{HCO}_3^-}$ , pmol·min <sup>-1</sup> ·mm <sup>-1</sup>	Investigators	Ref. No.
<i>HCO<sub>3</sub><sup>-</sup> ~ 10 mM (F<sub>v</sub> ~ 8 nl/min)</i>		
-12	Iacovitti et al.	46
-2	Levine et al.	57
10	Levine et al.	57
26.1	Chan et al.	20
31.9	(Model prediction)	
<i>HCO<sub>3</sub><sup>-</sup> ~ 25 mM (F<sub>v</sub> ~ 8 nl/min)</i>		
6	Levine et al.	57
7	Levine	56
10	Iacovitti et al.	46
15.5	Kunau and Walker	54
41.4	Kunau and Walker	54
53	Levine et al.	57
70.2	Chan et al.	20
75.9	Chan et al.	20
74.2	(Model prediction)	

F <sub>v</sub> , nl/min	$J_{\text{HCO}_3^-}$ , pmol·min <sup>-1</sup> ·mm <sup>-1</sup>	Investigators	Ref. No.
<i>HCO<sub>3</sub><sup>-</sup> ~ 10 mM</i>			
7→24	-12→-48	Iacovitti et al.	46
8→25	-2→-26	Levine et al.	57
8→25	10→11	Levine et al.	57
5→10→20	17→26→55	Chan et al.	20
8→12→24	32→30→29	(Model prediction)	
<i>HCO<sub>3</sub><sup>-</sup> ~ 25 mM</i>			
8→25	6→-54	Levine et al.	57
10→20	7→-4	Levine	56
7→24	10→-29	Iacovitti et al.	46
8→25	53→91	Levine et al.	57
5→10→20	66→76→65	Chan et al.	20
10→20→30	70→77→62	Chan et al.	20
8→12→24	74→71→67	(Model prediction)	

Model predictions have been calculated by using a modified model, in which lengths of early and late distal tubules were shortened to 0.5 cm and 0.7 cm, respectively, to adapt to microperfusion experiments. F<sub>v</sub>, flow rate. Constituents of perfusate were (in mM) 56 Na<sup>+</sup>, 2 K<sup>+</sup>, 48 Cl<sup>-</sup>, 10 HCO<sub>3</sub><sup>-</sup>, pH 7.02, and 22 urea for HCO<sub>3</sub><sup>-</sup> ~ 10 mM calculations and 56 Na<sup>+</sup>, 2 K<sup>+</sup>, 33 Cl<sup>-</sup>, 25 HCO<sub>3</sub><sup>-</sup>, pH 7.42, and 22 urea for HCO<sub>3</sub><sup>-</sup> ~ 25 mM calculations.

Incorporation of H-ATPase in the luminal membrane of the distal tubule is based on pharmacological evidence that luminal application of bafilomycin (a specific inhibitor of vacuolar H-ATPase) reduced HCO<sub>3</sub><sup>-</sup> reabsorption by 36 and 47% in the early and late distal tubules, respectively (76). Vacuolar H-ATPase is an electrogenic proton translocating ATPase that was originally identified in the intracellular vacuolar systems of eukaryotic cells. In the renal distal tubule, Brown et al. (13, 14) have demonstrated the presence of vacuolar H-ATPase immunocytochemically. They localized vacuolar H-ATPase in the luminal membrane of the early subsegment; in the late subsegment, they found immunoreactivity in the luminal membrane of

type A intercalated cells and in the basolateral membrane of type B intercalated cells. Unfortunately, studies specifically addressing the transport kinetics of vacuolar H-ATPase in the distal tubule are not available. Therefore, we have adopted the model of H-ATPase in turtle bladder (3), the kinetics of which have been extensively studied. This approach is supported by the results of Gluck and Caldwell (40) that vacuolar H-ATPase purified from renal medulla (which contains

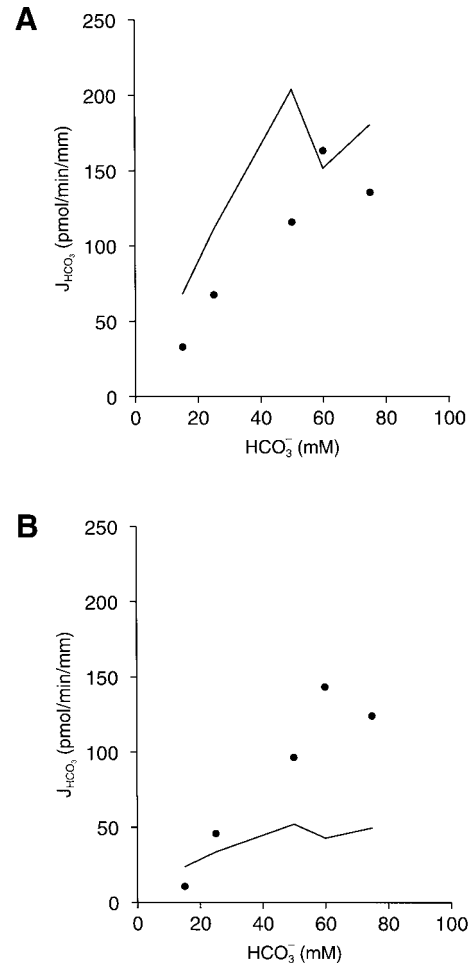


Fig. 12. Effect of luminal  $\text{HCO}_3^-$  concentration on  $\text{HCO}_3^-$  reabsorption rate. A:  $\text{HCO}_3^-$  reabsorption rate ( $J_{\text{HCO}_3^-}$ ) in the early distal tubule when it is perfused with various  $\text{HCO}_3^-$  concentrations (from 15 mM to 75 mM). Model prediction (solid line) is plotted together with experimental measurements (●; Ref. 76). B: results for the late distal tubule. The late distal tubule has been separated from the early distal tubule and has been perfused directly with test solutions (76). Constituents of the perfusate solution are 70 mM Na<sup>+</sup>, 1.86 mM K<sup>+</sup>, 56.86 mM Cl<sup>-</sup>, 15 mM HCO<sub>3</sub><sup>-</sup>, pH 7.20, and 78 mM urea; 70 mM Na<sup>+</sup>, 1.86 mM K<sup>+</sup>, 46.86 mM Cl<sup>-</sup>, 25 mM HCO<sub>3</sub><sup>-</sup>, pH 7.42, and 78 mM urea; 70 mM Na<sup>+</sup>, 1.86 mM K<sup>+</sup>, 21.86 mM Cl<sup>-</sup>, 50 mM HCO<sub>3</sub><sup>-</sup>, pH 7.72, and 78 mM urea; 146 mM Na<sup>+</sup>, 1.86 mM K<sup>+</sup>, 87.86 mM Cl<sup>-</sup>, 60 mM HCO<sub>3</sub><sup>-</sup>, pH 7.80, and 78 mM urea; and 146 mM Na<sup>+</sup>, 1.86 mM K<sup>+</sup>, 72.86 mM Cl<sup>-</sup>, 75 mM HCO<sub>3</sub><sup>-</sup>, pH 7.89, and 78 mM urea. Flow rate is 8 nl/min, and the bath solution has the same composition as in the legend for Table 5. It should be noted that Na<sup>+</sup> concentration is abruptly increased from 70 to 146 mM when  $\text{HCO}_3^-$  concentration is changed from 50 to 60 mM. This change in perfusate Na<sup>+</sup> concentration is probably responsible for the deflections in the model prediction in this  $\text{HCO}_3^-$  range.

intercalated cells) had basic kinetics that are similar to H-ATPases from other tissues in terms of pH dependency, substrate specificity, and Michaelis-Menten constant ( $K_m$ ) for ATP.

Schwartz et al. (71) demonstrated  $\text{Cl}^-/\text{HCO}_3^-$  exchange activity in the basolateral side of type A intercalated cells and in the apical side of type B intercalated cells. In type A intercalated cells, pharmacological and immunocytochemical evidence demonstrates that the activity is mediated by AE1 isoform of the anion exchanger gene family (1, 70). Transport kinetics of the AE1 isoform had been extensively studied using human red blood cell membranes. Most experiments had been conducted at low temperatures ( $\sim 0^\circ\text{C}$ ), because transport velocity becomes smaller and, therefore, suitable for measurements. Those experiments had revealed features such as asymmetric substrate affinities (43), self inhibition (i.e., inhibition of transport velocity at high substrate concentrations; Ref 43), and tunneling (i.e., movement of the anion through the exchanger without a conformational change; Ref. 33). We have been able to incorporate the feature of asymmetric substrate affinities and self inhibition in the present model owing to the recent experiments that addressed these features at body temperature (36, 49). However, similar data for tunneling are lacking, and extrapolation from low-temperature data is difficult because transport via anion exchanger exhibit complicated temperature dependency (12, 24). Therefore, the small effect of tunneling with physiological range of substrate concentrations (33) is not taken into account in the present model.

In type B intercalated cells, immunocytochemical studies detect none of the anion exchanger isoforms (AE1–AE3), and the molecular nature that mediates the apical  $\text{Cl}^-/\text{HCO}_3^-$  exchange is presently unclear (1, 70). Although detailed kinetic information about this  $\text{Cl}^-/\text{HCO}_3^-$  exchange is not available, experiments by Furuya et al. (34) showed in rabbit cortical collecting duct that the transport rate is dependent on luminal  $\text{Cl}^-$  with  $K_m$  of 18.7 mM (when luminal  $\text{HCO}_3^-$  is 25 mM). This  $K_m$  is comparable to the value of 16.6 mM that is predicted<sup>11</sup> from the present model. Therefore, we have assumed that transport kinetics of apical  $\text{Cl}^-/\text{HCO}_3^-$  in type B intercalated cells can also be approximated by this diagram.

Incorporation of  $\text{Cl}^-$  channel in basolateral membranes of intercalated cells is based on electrophysiological studies with rabbit distal tubule (64) and collecting duct (34, 50, 51, 64). For example, Muto et al. (64) showed that reducing the bath  $\text{Cl}^-$  concentration by 10-fold (from 120 to 12 mM) depolarized basolateral potential difference by 37.9 and 25.7 mV in type A and type B intercalated cells, respectively. On the other

hand, raising the bath K concentration by 10-fold (from 5 to 50 mM) depolarized basolateral potential only by 4.7 mV (in type A intercalated cells) and 3.1 mV (in type B intercalated cells). These results indicate that basolateral membranes of both types of intercalated cells are predominantly  $\text{Cl}^-$  selective. In contrast to basolateral membranes, apical membranes of intercalated cells are devoid of significant ion conductances, as indicated by fractional resistance of apical membranes [ $fR_a = R_a/(R_a + R_{bl})$ ] being near unity (50, 51, 64).

The basolateral Na/H exchanger and anion exchanger in the model tubule have been incorporated for practical reasons. Without these activities, solution of the model equations often led to unrealistic results, such as negative cytosolic  $\text{HCO}_3^-$  concentrations, when boundary conditions are varied to match experimental conditions. Although functional evidence for these transport activities is not available (probably for technical reasons), there is immunocytochemical evidence for the presence of NHE1 in distal convoluted tubule cells (9). However, immunoreactivity for AE1 is absent in both distal convoluted tubule cells and principal cells (74). Therefore, in the future it may become necessary to replace these anion exchangers by other  $\text{HCO}_3^-$ -extruding mechanisms (such as the Na- $\text{HCO}_3^-$  cotransporter) as more experimental data accumulate.

We have not incorporated H-K-ATPase activity in the present model, because luminal application of SCH-28080 (an inhibitor of H-K-ATPase) does not affect  $\text{HCO}_3^-$  reabsorption in either early or late distal tubules (76). Although H-K-ATPase plays an important role in increasing the  $\text{H}^+$  secretion in pathological states such as K depletion (81), it appears to have an insignificant role in acid-base transport in the normal state.

*Modeling the bicarbonate buffer system.* There is controversy about  $\text{Pco}_2$  levels in renal cortical structures. Early works on urinary acidification mechanism took it for granted that  $\text{Pco}_2$  in renal cortex is equal to that in systemic blood (62). However, this assumption was challenged by subsequent studies that directly measured cortical  $\text{Pco}_2$  with micro-Severinghaus electrodes (29, 30, 37). For example, DuBose et al. (30) reported that  $\text{Pco}_2$  levels in distal tubular fluid (67.1 Torr), peritubular vessels (64.8 Torr), and proximal tubular fluid (65.1 Torr) were significantly higher than those in systemic artery (39.2 Torr) and renal vein (41.1 Torr). Such a prominent  $\text{Pco}_2$  gradient between renal cortex and systemic blood appears difficult to explain, if we recall the highly diffusible nature of the  $\text{CO}_2$  molecule and the liberal blood supply to the kidney. Actually, quantitative arguments had excluded simple explanations such as 1) generation of  $\text{CO}_2$  by the addition of reabsorbed  $\text{HCO}_3^-$  to peritubular blood, 2) generation of  $\text{CO}_2$  in the tubular fluid by secreted  $\text{H}^+$ , and 3) generation of  $\text{CO}_2$  by tissue metabolism (8). More involved mathematical models had been required to account for the presumed  $\text{Pco}_2$  difference (6, 8). In the present model, we have followed the results of a more recent study by de Mello-Aires et al. (26), who reinvestigated the issue and confirmed the earlier as-

<sup>11</sup>Transport velocities have been calculated with luminal  $\text{HCO}_3^-$  of 25 mM, cytosolic  $\text{Cl}^-$  of 46 mM, cytosolic  $\text{HCO}_3^-$  of 18 mM, and varying luminal  $\text{Cl}^-$  concentrations; and the  $K_m$  has been determined as the luminal  $\text{Cl}^-$  concentration at which transport velocity becomes one-half of the value with luminal  $\text{Cl}^-$  concentration of 150 mM.

sumption that cortical  $P_{CO_2}$  is equal to that of systemic blood. By using micro-Severinghaus electrodes that contained carbonic anhydrase in the inner buffer solution, these investigators showed that  $P_{CO_2}$  levels in cortical structures (for example, 41.5 Torr in proximal tubule) were not different from those in renal vein (40.6 Torr) and carotid artery (38.8 Torr). When carbonic anhydrase was removed from electrodes,  $P_{CO_2}$  values in cortical structures apparently increased, and a significant portion of the measurements fell into the range of 50–60 Torr, consequently resembling the results of DuBose et al. (30). On the basis of these results, they argued that 1) when carbonic anhydrase is absent, there may exist a  $P_{CO_2}$  gradient in the inner buffer solution of the electrode due to its small tip size; 2) this  $P_{CO_2}$  gradient can deteriorate the reliability of  $P_{CO_2}$  measurement with these electrodes; and 3) this problem is circumvented by incorporating carbonic anhydrase in the electrode, because carbonic anhydrase is known to facilitate the diffusion of  $CO_2$  in fluid layers (60). We have considered that these experimental results and arguments are convincing and have assumed that  $P_{CO_2}$  values in cortical structures are equal to that of systemic blood.

Estimation of disequilibrium pH is dependent on the level of  $P_{CO_2}$ .<sup>12</sup> Therefore, it is understandable that conflicting results of  $P_{CO_2}$  led to conflicting estimation of disequilibrium pH. Investigators who maintain the position that there is no significant  $P_{CO_2}$  gap between tubular fluid and systemic blood supported the presence of disequilibrium pH in the distal tubular fluid (62), whereas investigators taking the opposite position denied the establishment of disequilibrium pH (28). The present model is consistent with the conclusion of the former investigators, due to our assumption about  $P_{CO_2}$  in cortical structures.

*Comparison with microperfusion experiments.* Given the greatly diversified results of microperfusion experiments, it is certain that no model tubule would simu-

late all of them with a single set of model parameters. The present model, whose parameters have been selected to fit free-flow micropuncture experiments, simulates properly a subset of microperfusion experiments (20, 54) that report rates of  $HCO_3^-$  reabsorption similar to those in micropuncture experiments. As an attempt to fit the other groups of microperfusion experiments, we have heuristically adjusted model parameters and found that by increasing the activities of transporters in type B intercalated cells we could simulate those experiments (46, 56, 57) that showed  $HCO_3^-$  secretion in the normal state and flow-dependent decrease in  $HCO_3^-$  reabsorption (equivalently, increase in  $HCO_3^-$  secretion). However, it is clear that modification of parameters only in type B intercalated cells cannot resolve all the diversities among microperfusion experiments. For example, it cannot explain the flow-dependent increase in  $HCO_3^-$  reabsorption in some experiments (20, 57). Furthermore, it cannot explain the more general observation that in microperfusion experiments transepithelial transport of  $Na^+$ ,  $K^+$ , and water is considerably diminished compared with micropuncture experiments (61). Therefore, we speculate that the origin of these diversities is most likely multifactorial, one of the mechanisms being altered activity of type B intercalated cells. Other proposed factors<sup>13</sup> are different levels of hydration and protein intake of experimental animals (54) and an unidentified component present in native tubular fluid but missing from artificial perfusate (61). Obviously, further experimental data addressing the nature of these mechanisms and their quantitative effects on individual transporters are required to update the model to simulate all of the details of microperfusion experiments.

## REFERENCES

1. **Alper SL.** The band 3-related anion exchanger (AE) gene family. *Annu Rev Physiol* 53: 549–564, 1991.
2. **Amemiya M, Loffing J, Löscher M, Kaissling B, Alpern RJ, and Moe OW.** Expression of NHE-3 in the apical membrane of rat renal proximal tubule and thick ascending limb. *Kidney Int* 48: 1206–1215, 1995.
3. **Andersen OS, Silveira JEN, and Steinmetz PR.** Intrinsic characteristics of the proton pump in the luminal membrane of a tight urinary epithelium. *J Gen Physiol* 86: 215–234, 1985.
4. **Aronson PS, Nee J, and Suhm MA.** Modifier role of internal  $H^+$  in activating the  $Na^+H^+$  exchanger in renal microvillus membrane vesicles. *Nature* 299: 161–163, 1982.
5. **Aronson PS, Suhm MA, and Nee J.** Interaction of external  $H^+$  with the  $Na^+H^+$  exchanger in renal microvillus membrane vesicles. *J Biol Chem* 258: 6767–6771, 1983.
6. **Atherton LJ, Deen WM, Maddox DA, and Gennari FJ.** Analysis of the factors influencing peritubular  $PCO_2$  in the rat. *Am J Physiol Renal Fluid Electrolyte Physiol* 247: F61–F72, 1984.

<sup>12</sup>We can see this by examining Eq. 3. On the left-hand side,  $G_{H_2CO_3}$  is actually negligible due to low concentration of luminal  $H_2CO_3$  ( $<8 \mu M$ ; see Tables 7 and 8) and small transepithelial  $H_2CO_3$  reabsorption rate ( $0.06 \text{ pmol} \cdot \text{min}^{-1} \cdot \text{distal tubule}^{-1}$ ). Specifically,  $H_2CO_3$  is  $0.41 \text{ pmol} \cdot \text{min}^{-1} \cdot \text{tubule}^{-1}$ , and  $G_{H_2CO_3}$  is  $-70.0 \text{ pmol} \cdot \text{min}^{-1} \cdot \text{tubule}^{-1}$  in the basic state. Therefore, we can drop  $G_{HCO_3}$  in Eq. 3, and after rearrangement we have

$$[H_2CO_3] = \frac{k_h}{k_d} [CO_2] - \frac{1}{k_d} G_{HCO_3}$$

Incorporating this equation into Eq. 2

$$\text{pH} = 3.57 + \log_{10} \frac{[HCO_3^-]}{\frac{k_h}{k_d} \cdot [CO_2]} - \log_{10} \left( 1 - \frac{G_{HCO_3}}{k_d \cdot \frac{k_h}{k_d} \cdot [CO_2]} \right)$$

The last term in the above equation,  $-\log_{10} \left( 1 - \frac{G_{HCO_3}}{k_d \cdot \frac{k_h}{k_d} \cdot [CO_2]} \right)$

shows the difference between the disequilibrium pH and the equilibrium pH. Therefore, discussion on the existence of disequilibrium pH is greatly affected by the estimation of  $[CO_2]$  (or  $P_{CO_2}$ ).

<sup>13</sup>Although it is possible that absence of phosphate and ammonium buffer systems in these experiments had contributed to the reduced rate of  $HCO_3^-$  reabsorption (17), the present model estimates that fractions of  $HCO_3^-$  reabsorption ascribable to these buffer systems are 1.0 pmol/min for phosphate buffer and 5.9 pmol/min for ammonium buffer ( $G_{HPO_4}$  and  $G_{NH_3}$  in Table 6). Therefore, it is unlikely that absence of these buffer systems accounts for the large difference ( $\sim 50 \text{ pmol/min}$ ) of  $HCO_3^-$  reabsorption rate between microperfusion and free-flow micropuncture experiments.

7. Beck FX, Dörge A, Rick R, Schramm M, and Thurau K. Effect of potassium adaptation on the distribution of potassium, sodium, and chloride across the apical membrane of renal tubular cells. *Pflügers Arch* 409: 477–485, 1987.
8. Bidani A, Crandall ED, and DuBose TD Jr. Analysis of the determinants of renal cortical  $\text{PCO}_2$ . *Am J Physiol Renal Fluid Electrolyte Physiol* 247: F466–F474, 1984.
9. Biemesderfer D, Reilly RF, Exner M, Igarashi P, and Aronson PS. Immunocytochemical characterization of  $\text{Na}^+\text{-H}^+$  exchanger isoform NHE-1 in rabbit kidney. *Am J Physiol Renal Fluid Electrolyte Physiol* 263: F833–F840, 1992.
10. Biemesderfer D, Rutherford PA, Nagy T, Pizzonia JH, Abu-Alfa AK, and Aronson PS. Monoclonal antibodies for high-resolution localization of NHE3 in adult and neonatal rat kidney. *Am J Physiol Renal Physiol* 273: F289–F299, 1997.
11. Bookstein C, Xie Y, Rabenau K, Musch MW, McSwine RL, Rao MC, and Chang EB. Tissue distribution of  $\text{Na}^+\text{-H}^+$  exchanger isoforms NHE2 and NHE4 in rat intestine and kidney. *Am J Physiol Cell Physiol* 273: C1496–C1505, 1997.
12. Brahm J. Temperature-dependent changes of chloride transport kinetics in human red cells. *J Gen Physiol* 70: 283–306, 1977.
13. Brown D, Hirsch S, and Gluck S. An  $\text{H}^+\text{-ATPase}$  in opposite plasma membrane domains in kidney epithelial cell subpopulation. *Nature* 331: 622–624, 1988.
14. Brown D, Hirsch S, and Gluck S. Localization of a proton-pumping ATPase in rat kidney. *J Clin Invest* 82: 2114–2126, 1988.
15. Brown D, Zhu XL, and Sly WS. Localization of membrane-associated carbonic anhydrase type IV in kidney epithelial cells. *Proc Natl Acad Sci USA* 87: 7457–7461, 1990.
16. Capasso G, Jaeger P, Giebisch G, Guckian V, and Malnic G. Renal bicarbonate reabsorption in the rat. II. Distal tubule load dependence and effect of hypokalemia. *J Clin Invest* 80: 409–414, 1987.
17. Capasso G, Kinne R, Malnic G, and Giebisch G. Renal bicarbonate reabsorption in the rat. I. Effect of hypokalemia and carbonic anhydrase. *J Clin Invest* 78: 1558–1567, 1986.
18. Chambrey R, Achard JM, St John PL, Abrahamson DR, and Warnock DG. Evidence for an amiloride-insensitive  $\text{Na}^+\text{-H}^+$  exchanger in rat renal cortical tubules. *Am J Physiol Cell Physiol* 273: C1064–C1074, 1997.
19. Chambrey R, Warnock DG, Podevin RA, Bruneval P, Mandet C, Bélaïr MF, Bariéty J, and Paillard M. Immunolocalization of the  $\text{Na}^+\text{-H}^+$  exchanger isoform NHE2 in rat kidney. *Am J Physiol Renal Physiol* 275: F379–F386, 1998.
20. Chan YL, Malnic G, and Giebisch G. Renal bicarbonate reabsorption in the rat. III. Distal tubule perfusion study of load dependence and bicarbonate permeability. *J Clin Invest* 84: 931–938, 1989.
21. Chang H and Fujita T. A kinetic model of the thiazide-sensitive  $\text{Na-Cl}$  cotransporter. *Am J Physiol Renal Physiol* 276: F952–F959, 1999.
22. Chang H and Fujita T. A numerical model of the renal distal tubule. *Am J Physiol Renal Physiol* 276: F931–F951, 1999.
23. Chang YL, Malnic G, and Giebisch G. Passive driving forces of proximal tubular fluid and bicarbonate transport: gradient dependence of  $\text{H}^+$  secretion. *Am J Physiol Renal Fluid Electrolyte Physiol* 245: F622–F633, 1983.
24. Chow EIH, Crandall ED, and Forster RE. Kinetics of bicarbonate-chloride exchange across the human red blood cell membrane. *J Gen Physiol* 68: 633–652, 1976.
25. Claveau D, Pellerin I, Leclerc M, and Brunette MG. Characterization of the  $\text{Na}^+\text{-H}^+$  exchanger in the luminal membrane of the distal nephron. *J Membr Biol* 165: 265–274, 1998.
26. De Mello-Aires M, Lopes MJ, and Malnic G.  $\text{PCO}_2$  in renal cortex. *Am J Physiol Renal Fluid Electrolyte Physiol* 259: F357–F365, 1990.
27. Dobyán DC and Bulger RE. Renal carbonic anhydrase. *Am J Physiol Renal Fluid Electrolyte Physiol* 243: F311–F324, 1982.
28. DuBose TD Jr, Pucacco LR, and Carter NW. Determination of disequilibrium pH in the rat kidney in vivo: evidence for hydrogen secretion. *Am J Physiol Renal Fluid Electrolyte Physiol* 240: F138–F146, 1981.
29. DuBose TD Jr, Pucacco LR, Lucci MS, and Carter NW. Micropuncture determination of pH,  $\text{PCO}_2$ , and total  $\text{CO}_2$  concentration in accessible structures of the rat renal cortex. *J Clin Invest* 64: 476–482, 1979.
30. DuBose TD Jr, Pucacco LR, Seldin DW, Carter NW, and Kokko JP. Direct determination of  $\text{PCO}_2$  in the rat renal cortex. *J Clin Invest* 62: 338–348, 1978.
31. Falke JJ, Kanés KJ, and Chan SI. The kinetic equation for the chloride transport cycle of band 3. *J Biol Chem* 260: 9545–9551, 1985.
32. Flessner MF, Wall SM, and Knepper MA. Permeabilities of rat collecting duct segments to  $\text{NH}_3$  and  $\text{NH}_4$ . *Am J Physiol Renal Fluid Electrolyte Physiol* 260: F264–F272, 1991.
33. Fröhlich O. Relative contributions of the slippage and tunneling mechanisms to anion net efflux from human erythrocytes. *J Gen Physiol* 84: 877–893, 1984.
34. Furuya H, Breyer MD, and Jacobson HR. Functional characterization of  $\alpha$ - and  $\beta$ -intercalated cell types in rabbit cortical collecting duct. *Am J Physiol Renal Fluid Electrolyte Physiol* 261: F377–F385, 1991.
35. Garg LC and Maren TH. The rates of hydration of carbon dioxide and dehydration of carbonic acid at 37°. *Biochim Biophys Acta* 261: 70–76, 1972.
36. Gasbjerg PK, Knauf PA, and Brahm J. Kinetics of bicarbonate transport in human red blood cell membranes at body temperature. *J Gen Physiol* 108: 565–575, 1996.
37. Gennari FJ, Cafisch CR, Johns C, Maddox DA, and Cohen JJ.  $\text{PCO}_2$  measurements in surface proximal tubules and peritubular capillaries of the rat kidney. *Am J Physiol Renal Fluid Electrolyte Physiol* 242: F78–F85, 1982.
38. Gillen CM, Brill S, Payne JA, and Forbush B III. Molecular cloning and functional expression of the K-Cl cotransporter from rabbit, rat, and human. *J Biol Chem* 271: 16237–16244, 1996.
39. Glabman S, Klose RM, and Giebisch G. Micropuncture study of ammonia excretion in the rat. *Am J Physiol* 205: 127–132, 1963.
40. Gluck S and Caldwell J. Immunoaffinity purification and characterization of vacuolar  $\text{H}^+\text{-ATPase}$  from bovine kidney. *J Biol Chem* 262: 15780–15789, 1987.
41. Goldman DE. Potential, impedance, and rectification in membranes. *J Gen Physiol* 27: 37–60, 1943.
42. Good DW and Burg MB. Ammonia production by individual segments of the rat nephron. *J Clin Invest* 73: 602–610, 1984.
43. Gunn RB and Fröhlich O. Asymmetry in the mechanism for anion exchange in human red blood cell membranes. *J Gen Physiol* 74: 351–374, 1979.
44. Hayes CP, Mayson JS Jr, Owen EE, and Robinson RR. A micropuncture evaluation of renal ammonia excretion in the rat. *Am J Physiol* 207: 77–83, 1964.
45. Hille B. *Ionic Channels of Excitable Membranes* (2nd ed.). Sunderland, MA: Sinauer, 1992.
46. Iacovitti M, Nash L, Peterson LN, Rochon J, and Levine DZ. Distal tubule bicarbonate accumulation in vivo. *J Clin Invest* 78: 1658–1665, 1986.
47. Jaeger P, Karlmark B, and Giebisch G. Ammonium transport in rat cortical tubule: relationship to potassium metabolism. *Am J Physiol Renal Fluid Electrolyte Physiol* 245: F593–F600, 1983.
48. Katz AI, Doucet A, and Morel F. Na-K-ATPase activity along the rabbit, rat, and mouse nephron. *Am J Physiol Renal Fluid Electrolyte Physiol* 237: F114–F120, 1979.
49. Knauf PA, Gasbjerg PK, and Brahm J. The asymmetry of chloride transport at 38°C in human red blood cell membranes. *J Gen Physiol* 108: 577–589, 1996.
50. Koeppen BM. Conductive properties of the rabbit outer medullary collecting duct: inner stripe. *Am J Physiol Renal Fluid Electrolyte Physiol* 248: F500–F506, 1985.
51. Koeppen BM. Conductive properties of the rabbit outer medullary collecting duct: outer stripe. *Am J Physiol Renal Fluid Electrolyte Physiol* 250: F70–F76, 1986.
52. Krahn TA and Weinstein WA. Acid/base transport in a model of the proximal tubule brush border: impact of carbonic anhydrase. *Am J Physiol Renal Fluid Electrolyte Physiol* 270: F344–F355, 1996.

53. **Kriz W and Bankir L.** A standard nomenclature for structures of the kidney. *Kidney Int* 33: 1–7, 1988.
54. **Kunau RT Jr and Walker KA.** Total CO<sub>2</sub> absorption in the distal tubule of the rat. *Am J Physiol Renal Fluid Electrolyte Physiol* 252: F468–F473, 1987.
55. **Läuger P.** *Electrogenic Ion Pumps*. Sunderland, MA: Sinauer, 1991.
56. **Levine DZ.** An in vivo microperfusion study of distal tubule bicarbonate reabsorption in normal and ammonium chloride rats. *J Clin Invest* 75: 588–595, 1985.
57. **Levine DZ, Iacovitti M, Nash L, and Vidorpe D.** Secretion of bicarbonate by rat distal tubules in vivo. *J Clin Invest* 81: 1873–1878, 1988.
58. **Levine SA, Montrose MH, Tse CM, and Donowitz M.** Kinetics and regulation of three cloned mammalian Na<sup>+</sup>/H<sup>+</sup> exchangers stably expressed in a fibroblast cell line. *J Biol Chem* 268: 25527–25535, 1993.
59. **Liu D, Kennedy SD, and Knauf PA.** Source of transport site asymmetry in the band 3 anion exchange protein determined by NMR measurements of external Cl<sup>-</sup> affinity. *Biochemistry* 35: 15228–15235, 1996.
60. **Malnic G.** CO<sub>2</sub> equilibria in renal tissue. *Am J Physiol Renal Fluid Electrolyte Physiol* 239: F307–F318, 1980.
61. **Malnic G, Berliner RW, and Giebisch G.** Distal perfusion studies: transport stimulation by native tubule fluid. *Am J Physiol Renal Fluid Electrolyte Physiol* 258: F1523–F1527, 1990.
62. **Malnic G, de Mello-Aires M, and Giebisch G.** Micropuncture study of renal tubular hydrogen ion transport in the rat. *Am J Physiol* 222: 147–158, 1972.
63. **Malnic G and Giebisch G.** Some electrical properties of distal tubular epithelium in the rat. *Am J Physiol* 223: 797–808, 1972.
64. **Muto S, Yasoshima K, Yoshitomi K, Imai M, and Asano Y.** Electrophysiological identification of alpha- and beta-intercalated cells and their distribution along the rabbit distal nephron segments. *J Clin Invest* 86: 1829–1839, 1990.
65. **Orlowski J and Grinstein S.** Na<sup>+</sup>/H<sup>+</sup> exchangers of mammalian cells. *J Biol Chem* 272: 22373–22376, 1997.
66. **Palmer LG, Choe H, and Frindt G.** Is the secretory K channel in the rat CCT ROMK? *Am J Physiol Renal Physiol* 273: F404–F410, 1997.
67. **Pizzonia JH, Biemesderfer D, Abu-Alfa AK, Wu MS, Exner M, Isenring P, Igarashi P, and Aronson PS.** Immunohistochemical characterization of Na<sup>+</sup>/H<sup>+</sup> exchanger isoform NHE4. *Am J Physiol Renal Physiol* 275: F510–F517, 1998.
68. **Preisig PA and Alpern RJ.** Contributions of cellular leak pathways to net NaHCO<sub>3</sub> and NaCl absorption. *J Clin Invest* 83: 1859–1867, 1989.
69. **Press WH, Flannery BP, Teukolsky SA, and Vetterling WT.** *Numerical Recipes in C*. Cambridge, MA: Cambridge Univ. Press, 1988.
70. **Schuster VL.** Function and regulation of collecting duct intercalated cells. *Annu Rev Physiol* 55: 267–288, 1993.
71. **Schwartz GJ, Barasch J, and Al-Awqati Q.** Plasticity of functional epithelial polarity. *Nature* 318: 368–371, 1985.
72. **Schwartz GJ, Kittelberger AM, Barnhart DA, and Vijayakumar S.** Carbonic anhydrase IV is expressed in H<sup>+</sup>-secreting cells of rabbit kidney. *Am J Physiol Renal Physiol* 278: F894–F904, 2000.
73. **Strieter J, Stephenson JL, Giebisch G, and Weinstein AM.** A mathematical model of the rabbit cortical collecting tubule. *Am J Physiol Renal Fluid Electrolyte Physiol* 263: F1063–F1075, 1992.
74. **Verlander JW, Madsen KM, Low PS, Allen DP, and Tisher CC.** Immunocytochemical localization of band 3 protein in the rat collecting duct. *Am J Physiol Renal Fluid Electrolyte Physiol* 255: F115–F125, 1988.
75. **Wall SM and Koger LM.** NH<sub>4</sub><sup>+</sup> transport mediated by Na<sup>+</sup>-K<sup>+</sup>-ATPase in rat inner medullary collecting duct. *Am J Physiol Renal Fluid Electrolyte Physiol* 267: F660–F670, 1994.
76. **Wang T, Malnic G, Giebisch G, and Chan YL.** Renal bicarbonate reabsorption in the rat. IV. Bicarbonate transport mechanisms in the early and late distal tubule. *J Clin Invest* 91: 2776–2784, 1993.
77. **Weinstein AM.** A kinetically defined Na<sup>+</sup>/H<sup>+</sup> antiporter within a mathematical model of the rat proximal tubule. *J Gen Physiol* 105: 617–641, 1995.
78. **Weinstein AM.** A mathematical model of the inner medullary collecting duct of the rat: pathways for Na and K transport. *Am J Physiol Renal Physiol* 274: F841–F855, 1998.
79. **Weinstein AM.** A mathematical model of the outer medullary collecting duct of the rat. *Am J Physiol Renal Physiol* 279: F24–F45, 2000.
80. **Windhager EE and Giebisch G.** Electrophysiology of the nephron. *Physiol Rev* 45: 214–244, 1965.
81. **Wingo CS and Cain BD.** The renal H-K-ATPase: physiological significance and role in potassium homeostasis. *Annu Rev Physiol* 55: 323–347, 1993.
82. **Yip KP and Kurtz I.** NH<sub>3</sub> permeability of principal cells and intercalated cells measured by confocal fluorescence imaging. *Am J Physiol Renal Fluid Electrolyte Physiol* 269: F545–F550, 1995.
83. **Zahler R, Zhang ZT, Manor M, and Boron WF.** Sodium kinetics of Na,K-ATPase alpha isoforms in intact transfected HeLa cells. *J Gen Physiol* 110: 201–213, 1997.